Check for updates

JGR Solid Earth

RESEARCH ARTICLE
10.1029/2020JB021136

Key Points:

- This study confirmed global geomagnetic field behavior during Mid to Late Jurassic
- Our new, multiscale marine magnetic anomaly data revealed the crustal age of the oldest Pacific is ~Chron M42
- Newly discovered the Jurassic Disturbed Zone, bounded by M39–M41 isochrons represents the core of widely known the Jurassic Quiet Zone

Supporting Information:

- Supporting Information S1

Correspondence to:
M. Tominaga,
mtominaga@whoi.edu

Citation:
Tominaga, M., Tivey, M. A., & Sager, W. W. (2021). A new middle to Late Jurassic Geomagnetic Polarity Time Scale (GPTS) from a multiscale marine magnetic anomaly survey of the Pacific Jurassic Quiet Zone. *Journal of Geophysical Research: Solid Earth*, *126*, e2020JB021136. https://doi.org/10.1029/2020JB021136

Received 6 OCT 2020
Accepted 17 JAN 2021

© 2021. American Geophysical Union. All Rights Reserved.

A New Middle to Late Jurassic Geomagnetic Polarity Time Scale (GPTS) From a Multiscale Marine Magnetic Anomaly Survey of the Pacific Jurassic Quiet Zone

Masako Tominaga[1], Maurice A. Tivey[1], and William W. Sager[2]

[1]Department of Geology and Geophysics, Woods Hole Oceanographic Institution, Woods Hole, MA, USA, [2]Department of Earth and Atmospheric Sciences, University of Houston, Houston, TX, USA

Abstract The Geomagnetic Polarity Time Scale (GPTS) provides a basis for the geological timescale, quantifies geomagnetic field behavior, and gives a time framework for geologic studies. We build a revised Middle to Late Jurassic GPTS by using a new multiscale magnetic profile, combining sea surface, midwater, and autonomous underwater vehicle near-bottom magnetic anomaly data from the Hawaiian lineation set in the Pacific Jurassic Quiet Zone (JQZ). We correlate the new profile with a previously published contemporaneous magnetic sequence from the Japanese lineation set. We then establish geomagnetic polarity block models as a basis for our interpretation of the origin and nature of JQZ magnetic anomalies and a GPTS. A significant level of coherency between short-wavelength anomalies for both the Japanese and Hawaiian lineation magnetic anomaly sequences suggests the existence of a regionally coherent field during this period of rapid geomagnetic reversals. Our study implies the rapid onset of the Mesozoic Dipole Low from M42 through M39 and then a subsequent gradual recovery in field strength into the Cenozoic. The new GPTS, together with the Japanese sequence, extends the magnetic reversal history from M29 back in time to M44. We identify a zone of varying, difficult-to-correlate anomalies termed the Hawaiian Disturbed Zone, which is similar to the zone of low amplitude, difficult-to-correlate anomalies in the Japanese sequence termed the Low Amplitude Zone (LAZ). We suggest that the LAZ, bounded by M39–M41 isochrons, may in fact represent the core of what is more commonly known as the JQZ crust.

Plain Language Summary The western Pacific Ocean has by far the largest extent of Jurassic (145 to 180 Myr) ocean crust remaining in the world forming an important repository of the oldest oceanic crustal recording of geomagnetic field history. We use this magnetic record to establish a Geomagnetic Polarity Time Scale that forms the basis for the Geological Time Scale that quantifies Earth's geological evolution. Jurassic magnetism has been difficult to quantify because of its weak signal in the Pacific leading to its characterization as the Jurassic Quiet Zone with limited polarity reversals. In this study, we use a new approach by measuring magnetism in the Pacific Hawaiian magnetic sequence at multiple scales using sensors at the sea surface, on a deep towed sled and on a near-bottom autonomous underwater vehicle. We find a sequence of rapid magnetic reversals that can be correlated with a previous record obtained from the Pacific Japanese anomaly sequence. Superimposed on this reversal history is a longer wavelength variation in magnetic anomaly amplitude that suggests the Mid Jurassic indeed had a weak field intensity. Thus, the Jurassic magnetic field was weak and reversing polarity at much greater rates than any time since.

1. Introduction

Seafloor spreading marine magnetic anomalies provide the most continuous and comprehensive record of past geomagnetic field behavior extending back in time to ~180 Ma. This record enables us to better understand the approximate locations and timing of the formation of new tectonic plates from the breakup of the supercontinent Pangea (e.g., Bartolini & Larson, 2001; Boschman & van Hinsbergen, 2016; Coffin et al., 2000; Hilde et al., 1976; Lancelot, Larson, & Fisher, 1990; Lancelot, Larson, & Shipboard Scientific Party, 1990; Madrigal et al., 2016; Müller et al., 2016; Seton et al., 2012; Van Avendonk et al., 2017; N. Zhang & Zhong, 2011). Combining marine magnetic anomaly and terrestrial geomagnetic polarity records allows us to build a continuous and detailed Geomagnetic Polarity Time Scale (GPTS) to better calibrate

magnetostratigraphy and other stratigraphic records and thereby construct a comprehensive Geological Time Scale (e.g., Cande & Kent, 1992a, 1995; Cox, 1969; Gradstein et al., 2012; Heirtzler & Hayes, 1967; Larson & Hilde, 1975; Ogg et al., 2018). The GPTS not only provides a basis for the geological timescale but also enables us to quantify geomagnetic field behavior and infer connections between plate tectonics, geodynamo, and mantle dynamics. Geomagnetic polarity reversal frequencies and other statistical properties of the GPTS can also be used to constrain more realistic models of the geodynamo (e.g., Buffett, 2000; Coe et al., 2000; Dormy et al., 2000; Glatzmaier & Roberts, 1995; Takahashi et al., 2005).

The current GPTS ranges from the present back to Chron M29 (~157 Ma) time (Gradstein et al., 2012). However, the validity of the pre-M29, Mid Jurassic to Early Cretaceous GPTS model remains the subject of ongoing research (e.g., Ogg et al., 2018; Tominaga & Sager, 2010; Tominaga et al., 2008; Walker et al., 2013). The marine magnetic record from the present to Chron M29 shows that the geomagnetic field sometimes underwent frequent reversals through time, with the exception of the ~40-Myr long Cretaceous Normal Superchron (CNS) (84–124 Ma), a period that is globally characterized by a constant normal polarity (Cande & Kent, 1992a, 1995; Coe & Glatzmaier, 2006; Granot et al., 2007, 2012; Lowrie & Kent, 2004; Valet & Fournier, 2016). The current seafloor spreading marine magnetic record ends in the Mid to Late Jurassic when amplitudes of sea surface marine magnetic anomalies decrease and become undecipherable—a period characterized as the Jurassic Quiet Zone (JQZ) (Cande et al., 1978; Larson & Chase, 1972). Unlike the CNS, the JQZ record has been unclear. This is a result of limited marine and terrestrial records and difficult correlations among them. The JQZ is the oldest and deepest oceanic crust in the ocean basins today, making it challenging to access. Terrestrial magnetostratigraphic records are rarely continuous and often in highly tectonized Tethyan sedimentary formations (e.g., Lowrie & Channell, 1984; Przybylski, Ogg, et al., 2010). Work to date on the Pacific JQZ marine magnetic anomalies reveal low amplitude short-wavelength anomalies suggesting high reversal rates, higher than at any other time since (Sager et al., 1998; Tivey et al., 2006; Tominaga et al., 2015) and low field intensities (McElhinny & Larson, 2003; Tominaga et al., 2008). Without rock magnetic measurements and magnetostratigraphic correlations to validate the existence of JQZ polarity reversals, there is always a possibility that some of this behavior may also be field intensity fluctuations (e.g., Cande & Kent, 1992b).

To capture and quantify the Mid to Late Jurassic geomagnetic field history and to assess the origin and nature of the pre-M29 marine magnetic record, we present a new multiscale marine magnetic anomaly data set from the western Pacific basin. We use the results of a magnetic and seismic survey collected from the Jurassic to Middle Cretaceous to build a revised polarity time scale model for the Middle Jurassic to Early Cretaceous period. Our multiscale data set from the Hawaiian lineation set is novel by including sea surface, midwater, and near-source magnetic data, the latter acquired by the autonomous underwater vehicle (AUV) *Sentry*, to document the magnetic anomalies recorded in some of the oldest remaining in situ ocean crust. Combining these results with previous work in the Japanese lineation set allows us to assess the nature of Earth's magnetic field behavior recorded by contemporaneous JQZ ocean basins.

2. Background

2.1. The Evolution of the Western Pacific Plate

The Pacific plate was formed at the Phoenix–Izanagi–Farallon triple junction during the Mid Jurassic (175–180 Ma), likely as a consequence of a global plate reorganization related to the breakup of Pangea (Bartolini & Larson, 2001; Coffin et al., 2000). Three magnetic lineation sets, the Japanese, Hawaiian, and Phoenix, outline the early evolution of the Pacific plate as it expanded and moved northwards to its present location (Hilde et al., 1976; Larson & Chase, 1972; Nakanishi & Winterer, 1998; Nakanishi et al., 1992; Woods & Davies, 1982). Chron M29 is the oldest and most widely accepted coherent magnetic isochron in all three lineation sets and encloses a triangular area where the Pacific plate initially formed (Figure 1). Prior to Chron M29 is the JQZ, where magnetic anomalies are marked by low amplitudes with short wavelengths that make them difficult to correlate (Barrett & Keen, 1976; Cande et al., 1978; Handschumacher et al., 1988; Hayes & Rabinowitz, 1975; Heirtzler & Hayes, 1967; Hilde et al., 1976; Larson & Pitman, 1972; Sager et al., 1998; Tivey et al., 2006; Tominaga et al., 2008). Part of the reason for the weak sea surface magnetic anomalies and correlation difficulties is that the ocean floor is >6,000 m deep, yielding a large source-to-sensor distance. The region was also formed near the magnetic equator, which results in low anomaly

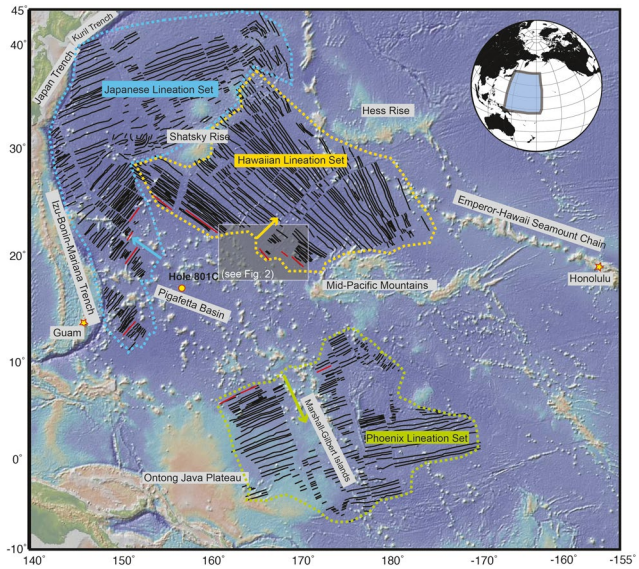

Figure 1. Map of the western Pacific showing the three previously identified magnetic lineation sets: Japanese, Hawaiian, and Phoenix (e.g., Nakanishi et al., 1989) and major seafloor geologic features, including subduction zones and seamount chains. Red line shows Chron M29. Arrows show general seafloor spreading directions. Underlying bathymetry is extracted from GMRT v3.7 (Ryan et al., 2009).

amplitudes, and it is currently in low latitudes, an area where diurnal noise results in a lower signal-to-noise ratio for sea surface surveys.

The western Pacific is also subject to widespread intraplate volcanism of Cretaceous age that impacts the entire western Pacific basin (Hamilton, 1956; Koppers, Staudigel, & Duncan, 2003; Koppers, Staudigel, Pringle, et al., 2003; Morgan, 1972; Ohira et al., 2017) (Figure 1). Seismic imaging studies suggest that there were late-stage volcanic features such as sills and lava flows throughout the western Pacific basin (Abrams et al., 1992; Feng, 2016; Kaneda et al., 2010; Stadler & Tominaga, 2015). Radiometric $^{40}Ar/^{39}Ar$ dating of seamounts in the Marcus-Wake and Magellan Seamount chains yield ages ranging from 75 to 125 Ma (e.g., Clouard & Bonneville, 2004; Koppers, Staudigel, & Duncan, 2003; Koppers, Staudigel, Pringle, et al., 2003; Saito & Ozima, 1977).

Ocean Drilling Program (ODP) Hole 801C, located at 18° 38.538′N, 156° 21.588′E within the Japanese magnetic lineation sequence (Figure 1) in the Pigafetta Basin, provides a key reference site for understanding the nature and evolution of western Pacific Jurassic crustal formation (Lancelot, Larson, & Fisher, 1990; Lancelot, Larson, & Shipboard Scientific Party, 1990; Plank et al., 2000). ODP 801C core samples give high-resolution $^{40}Ar/^{39}Ar$ dates for crustal basalts of 167.4 ± 1.4/3.4 Ma (internal/absolute error) (Koppers, Staudigel, & Duncan, 2003). Downhole wireline log-based volcanic facies analyses document that this part of the Pacific Jurassic crust was formed at a fast spreading ridge system (Pockalny & Larson, 2003). Wireline log and downhole magnetic anomaly data also reveal that multiple magnetic reversals are present in the oceanic basement (Tivey et al., 2005). These data analyses imply that the low magnetic anomaly amplitudes in the JQZ could be attributed to rapid magnetic reversals, leading to the potential superposition of overlapping, oppositely magnetized sequences within a vertical crustal section, thereby reducing the total effective magnetization of the crustal section (Steiner, 2001; Tivey et al., 2005).

2.2. The Mid Jurassic Marine Magnetic Record

Mesozoic ("M-series") marine magnetic anomalies were first mapped and correlated in the northeast Atlantic as the Keathley sequence (Vogt et al., 1971). Subsequent mapping and correlation of magnetic anomalies in the Pacific revealed a concurrent sequence of correlatable anomalies on several different sets of lineations (Larson & Chase, 1972), which allowed for a world-wide correlation of M-series anomalies to be constructed and added to the GPTS, previously established for the Late Cretaceous and Cenozoic by Heirtzler and & Hayes (1967). Revised Mesozoic timescales, primarily based on the faster spreading Pacific crust, were subsequently generated (Cande et al., 1978; Larson & Hilde, 1975; Nakanishi et al., 1989) with the most recent revisions by Channell et al. (1995), Tominaga and Sager (2010), and Malinverno et al. (2012).

While M-series anomalies are identified in the oldest parts of major ocean basins (e.g., Cooper et al., 1976; Gurevich et al., 2006; Hayes & Rabinowitz, 1975; Klitgord & Schouten, 1986; Leinweber & Jokat, 2012; Ramana et al., 1994, 2001; Roeser et al., 2002; Roest et al., 1992; Rybakov et al., 2000; Sager et al., 1992; Tominaga & Sager, 2010; Verhoef & Scholten, 1983; Vogt et al., 1971), the most complete sequence of Late to Mid Jurassic anomalies is in the western Pacific (Figure 1). The onset of the JQZ was first inferred from the disappearance of correlatable anomalies in both the Atlantic and Pacific (Cande et al., 1978; Larson & Chase, 1972; Larson & Hilde, 1975; Vogt & Einwich, 1979). The younger boundary of the JQZ has changed through time as anomaly resolution has improved from M22 (Larson & Chase, 1972), to M25 (Larson & Hilde, 1975), to the present, widely accepted M29 chron in the Pacific (Cande et al., 1978; Channell et al., 1995; Handschumacher et al., 1988; Kent & Gradstein, 1985).

A series of deep-tow magnetic surveys significantly improved the extent of correlatable anomalies in the Japanese lineation set (Sager et al., 1998; Tivey et al., 2006; Tominaga et al., 2008). Two long near-bottom

magnetic transects in the Pigafetta Basin were used to overcome the filtering effect of water depth by amplifying the crustal signal showing that anomalies can be correlated, possibly as far back in time as M44 (~170 Ma). One of these transects crosses ODP Hole 801C, and those downhole results were tied to the marine magnetic record (Tivey et al., 2006; Tominaga et al., 2008). These data from the Japanese lineation set suggest that the JQZ should be redefined in its temporal extent to the M38–M41 period where a minimum in anomaly amplitude is observed and is preceded by stronger amplitudes (Tivey et al., 2006; Tominaga et al., 2008). The decrease in the near-bottom magnetic anomaly amplitudes observed in the Japanese lineation set is consistent with the monotonic decrease in sea surface magnetic anomaly amplitudes seen from M19 toward M29 (Figure 3, Cande et al., 1978; Larson & Hilde, 1975; McElhinny & Larson, 2003). Taken together, these observations suggest that low field intensities were prevalent during the JQZ period compared to the overall higher paleointensity throughout CNS (Figure 2(a), Biggin & Thomas, 2003; Granot et al., 2012; Tauxe, 2006).

Several groups have reported Jurassic geomagnetic field reversals from terrestrial magnetostratigraphy (Ogg & Gutowski, 1995; Steiner et al., 1985, 1987), confirming polarity reversals during the M25–M38 period (Ogg et al., 2010; Przybylski, Głowniak, et al., 2010; Przybylski, Ogg, et al., 2010). More recent magnetostratigraphic and rock magnetic studies from European and South American basins also show magnetic reversals deeper in time, M38–M44 (e.g., Gipe, 2013; Llanos et al., 2019). Although these results appear to confirm the interpretation of rapid Jurassic reversals, the near-bottom Japanese lineation survey data (Sager et al., 1998; Tivey et al., 2006; Tominaga et al., 2008) are a record from only one spreading center. Records from other spreading centers are needed to verify that the Jurassic magnetic signal is present and coherent among these lineation sets from the JQZ period.

3. Methods

3.1. Sea Surface, Midtow (Midwater Level), and Sentry AUV Magnetic Data

We obtained ~4,600 km of sea surface magnetic profiles in the Pacific Hawaiian anomaly sequence during the TN272 cruise on *R/V Thomas G. Thompson* (December 2011 to January 2012) and the SKQ2014S2 cruise on *R/V Sikuliaq* (December 2014 to January 2015). The location of the survey profiles was carefully chosen to stay within the flowline of a single mid-ocean ridge spreading segment to avoid crossing fracture zones. Furthermore, the transect was located within a corridor between seamounts to minimize possible volcanic overprints (Figures 1 and 2). Sea surface magnetic profiles were acquired using a Marine Magnetics SeaSpy Overhauser total field magnetometer towed behind the ship with a sampling frequency of 1 Hz and a resolution of 0.1 nT (Lines 26, 3, 4, 479, and 51,038 in Figures 2 and 3). GPS navigation data were provided by the *R/V Sikuliaq* and *Thompson*'s Seapath navigation system.

In addition to the sea surface profiles, we obtained ~700 km of midwater towed marine magnetic profiles during the TN272 cruise. We used a 6,000-m-rated Marine Magnetics SeaSpy Overhauser total field magnetometer with a 0.1-nT resolution at 1-Hz sampling frequency. This midwater towed magnetometer was mounted directly onto the aluminum vehicle frame (TowCam) with a depth sensor and a separate Honeywell (HMR-2300) three-axis vector magnetometer (4 nT resolution) fixed on the tow-sled frame. The TowCam sled was towed along same survey track as the multichannel seismic (MCS) survey line and controlled to maintain an average 4.5 km water depth using the ship's 0.322-in. conducting cable and winch (Figures 2(a2)). The TowCam data were transmitted in real time to the ship over the cable using a digital subscriber link ethernet connection to monitor and adjust the flying depth in real time. The position of the midwater level magnetic data used the ship GPS navigation, the depth of the tow-sled, and wire pay-out to compute the layback of the sensor behind the ship. The vector HMR sensor data during turns and pitch and roll changes were used to estimate the induced magnetic field effects of the TowCam sled and correct the total magnetic field measured by the midwater towed magnetometer. Individual tows were organized into composite lines where they overlapped and then these were compiled into one single survey line (Figures 2 and 3).

Both sea surface and midwater profiles were corrected for diurnal variations using data obtained from geomagnetic observatories located in Guam and Hawaii. A diurnal correction for the survey site was extracted by time-shifting the diurnal time series from both Guam and Hawaii data sequences to the local survey

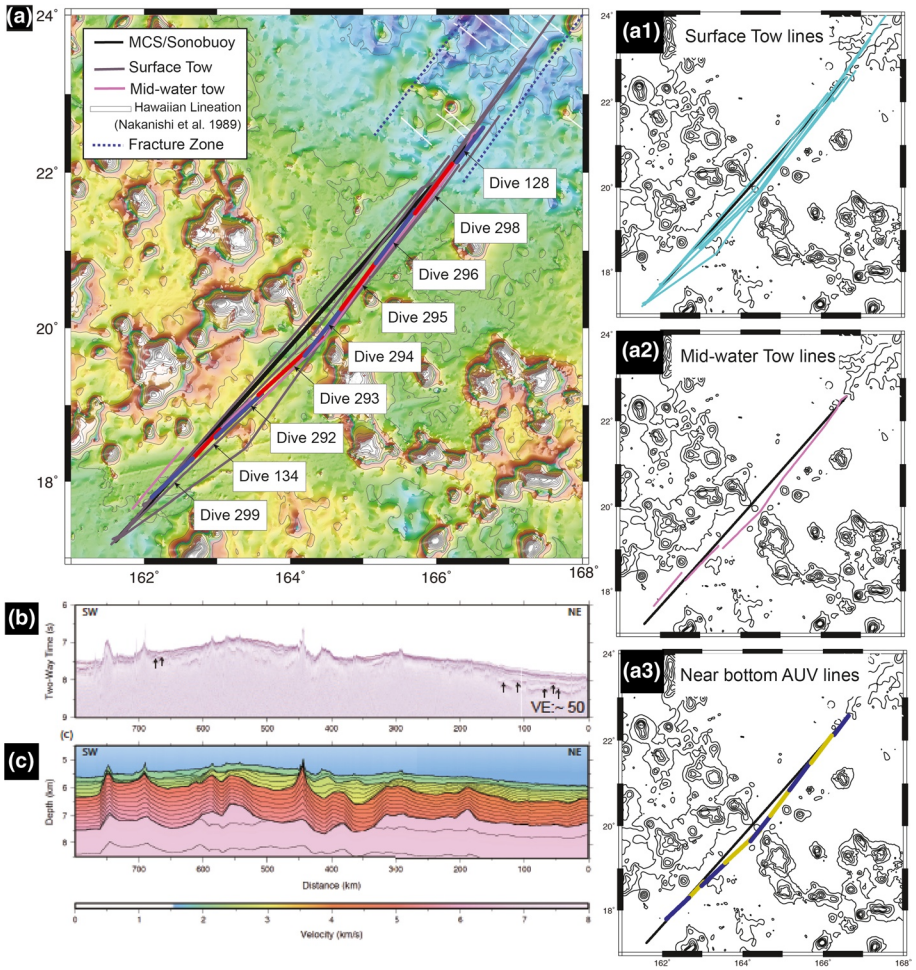

Figure 2. (a) Survey tracks of surface and midwater level towed magnetometers and autonomous underwater vehicle (AUV) Sentry plotted over satellite bathymetry (Smith & Sandwell, 1997). "Dive" indicates AUV Sentry dive. The black solid line is the Multichannel Seismic (MCS) survey line and used as a projection line for concatenating magnetic profiles (see text Section 3.3). Separate displays are (a1) sea surface magnetometer survey lines with the projection line; (a2) midtow magnetometer lines with the projection line; and (a3) AUV Sentry dive tracks with the projection line. (b) MCS reflection profile along the black solid line in panel (a). Small arrows indicate examples of volcanic sills in the sediment package (Feng, 2016; Feng et al., 2015). (c) Crustal velocity–thickness model based on sonobuoy refraction data along the MCS seismic line (Feng, 2016; Feng et al., 2015). Seismic layer 2, the igneous crustal layer that we have used as magnetic source geometry, is indicated in red-orange color. Green colored layers show sediment section with varying seismic velocities. Solid black curves indicate velocity contours. MCS, multichannel seismic.

longitude and conducting a linear interpolation of the observed range proportional to the latitude difference between observation site and the magnetic observatories for the duration of the cruises. The range in diurnal variation was ±20–80 nT with no major magnetic storms reported during the survey periods. The sea surface and midwater profiles were then corrected for the International Geomagnetic Reference Field (IGRF-12) (Thebault et al., 2015). The TowCam midwater magnetic anomaly data were continued upward from average 4.5 km towing depth to a constant 3.2 km water depth using a Fourier-domain method (Guspi, 1987). The upward-continued depth of 3.2 km was chosen as it is approximately half the water depth in the study area and is similar to the ~3 km depth of the midlevel of the Japanese lineation study (Tominaga et al, 2008). This depth is also approximately the average water depth for typical sea surface magnetic anomalies. These midwater data were also continued to the sea surface level using the Guspi (1987) method to help with anomaly correlations (Figure 3).

We obtained a total of 700 km of near-bottom marine magnetic profiles using the National Deep Submergence Facility AUV Sentry. AUV Sentry was equipped with an Applied Physics System three-axis fluxgate

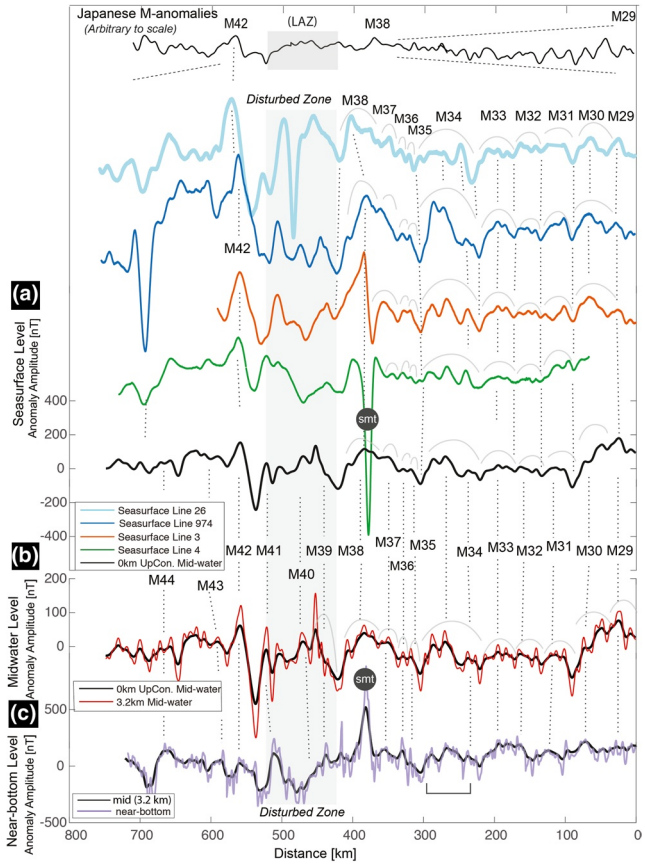

Figure 3. A summary of the correlation among the Japanese M-sequence anomalies and newly acquired marine magnetic anomaly profiles from the Hawaiian lineation set at different depths: (a) sea surface (Lines 26, 974, 3, and 4); (b) midwater (3.2 km water depth); and (c) near bottom (4.7 km water depth). Black curve at top is a composite sea surface magnetic anomaly from the Japanese lineation set (Tivey et al., 2006). Correlations of distinctive peaks and troughs of anomalies to show the "envelope" of each chron are shown with gray curves and dotted lines. The vertical gray bands denote the LAZ (Japanese anomalies) and HDZ (Hawaiian anomalies). The steps of correlating multiscale anomaly profiles using upward-continued profiles of near-bottom and midwater profiles are as follows: (1) between sea surface and midwater level correlation: the black thick solid line in (b) is upward-continued midwater level profile to sea surface level and used as a basis in correlating the sea surface and midwater profiles in (a); (ii) near-bottom and midwater level correlation: the black thick solid line in (c) is near-bottom level profile upward continued to midwater level and used as a basis for correlating the near-bottom and midwater profiles in between (b) and (c). "smt" denotes the anomaly disruption of a small seamount. LAZ, Low Amplitude Zone; HDZ, Hawaiian Disturbed Zone.

magnetic sensor (0.1 nT resolution) that was sampled at a 3–4-Hz rate. To correct for the magnetic effects of AUV Sentry, we adjusted the magnetic data for each dive using calibration coefficients calculated from data acquired during rotation of the vehicle on descent and ascent (e.g., Korenaga, 1995). Navigation was provided by ultrashort baseline sonar triangulation from the ship and doppler velocity logging on the AUV, flying at a mean survey height of ∼60 m altitude above the bottom. The magnetic profile from each AUV Sentry dive was corrected for diurnal variations and the regional field was removed using the IGRF model-12 (Thebault et al., 2015). Individual AUV Sentry magnetic profiles from the nine dives were then concatenated and a composite profile was continued upward to a constant −4.7 km water depth using the Guspi (1987) method (Figure 2(a)).

3.2. Crustal Structure Model

To assess the impact of Cretaceous volcanics on the Jurassic magnetic signal and to define sediment thickness for the magnetic modeling, we obtained seismic reflection and refraction data in conjunction with sea surface magnetic anomaly data acquisition during the TN272 cruise (Figure 2). MCS reflection profiles were acquired with a 600-m-long, 48-channel streamer, and two 110-in.^{3} GI guns, while crustal refractions were recorded by 50 sonobuoys over the ∼800 km survey transect, of which 42 were successful (Feng, 2016; Feng et al., 2015). MCS data were processed with ProMax software using band-pass filtering (15–150 Hz), trace editing, normal moveout correction, stacking, time migration, and automatic gain control (Feng, 2016; Feng et al., 2015). A crustal velocity model was constructed using the MCS and sonobuoy data (Zelt & Smith, 1992) (Figure 2(c)). Layer velocities and depths were adjusted through a forward-modeling approach to minimize the misfit between the predicted and picked travel times. In locations where the sonobuoy records were poor or absent, the velocity structure was interpolated using constraints on layer horizons from the MCS images (Figure 2(b) and 2(c)) (Feng, 2016; Feng et al., 2015).

3.3. Establishing a Polarity Block Model

We projected the sea surface, midwater, and near-bottom AUV magnetic profiles onto a common azimuth (∼45°) and subsampled other records at 0.02 km interval to match the AUV Sentry sample resolution (nominal cruising speed of 0.9 m/s at 60 m altitude above the seafloor) and to retain enough frequency range for subsequent Fourier-domain analyses. We first made magnetic anomaly correlations between multiple surface magnetic profiles. In this process, we identified distinctive anomalies (e.g., M42, M34, M35, and M36) (Tominaga et al., 2008), correlated them, and then matched the less-distinctive peaks in between (Figure 3). Polarity block models were constructed for each of the sea surface anomaly profiles and the composite midwater and Sentry AUV profiles (Figures 4 and 5). To establish a polarity block model, our first step for each profile was to use a Fourier-domain magnetization inversion approach (Parker & Huestis, 1974) to make a preliminary interpretation of the magnetization polarity distribution. Using the initial inversion results as an anchor, we refined the fit of observed and modeled anomalies with forward modeling (Parker, 1972) by adjusting the locations of polarity boundaries. We repeated this process until the normalized RMS misfit was reduced to less than 5 nT between the observed and calculated magnetic

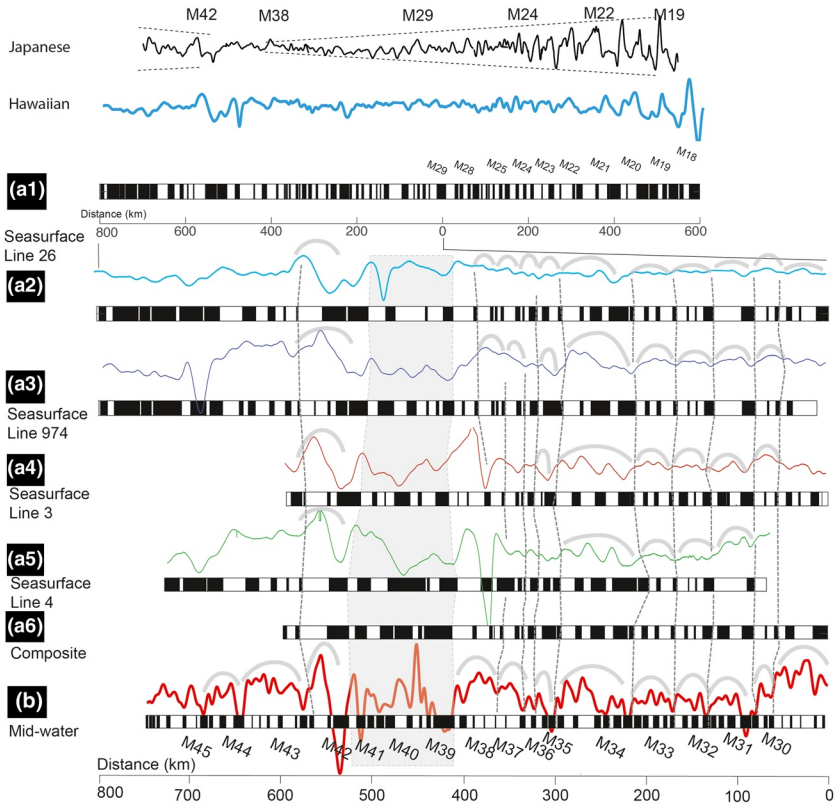

Figure 4. A comparison of polarity block models from four sea surface profiles and the midwater data collected during this study. The Japanese anomaly profile at the top of the figure is shown as a reference for anomaly envelopes (Tominaga et al., 2015). Black and white blocks show normal and reversed magnetization, respectively. Mesozoic anomalies observed in the western Pacific are positive anomalies defined by reversed polarity blocks because the crust was formed south of the current equator. Vertical dashed lines and gray band denote correlations between anomaly profiles, with the latter representing the Disturbed Zone discussed in the text. Gray lines above profiles show major anomaly envelopes. The vertical scale of each of the profiles is arbitrary. (a1) Japanese (black) and Hawaiian (blue) sea surface magnetic profiles (Tominaga et al., 2015) along with the Hawaiian Line 26 polarity block model of the complete reversal sequence from M18 to the end of the record. Note the expansion in scale of the 0–800 km section for the remaining profiles below. (a2–a5) Hawaiian sea surface profiles and their block models; (a6) a composite model based on profiles shown in (a2)–(a5) by the averaging approach (see Section 3.3). (b) The midwater level profile and polarity block model. All profiles are projected onto a single, straight profile along the MCS line (heavy solid line in Figure 2(a)). Distance in the plots refers to the distance based on the seismic line (i.e., Feng, 2016) for consistency with archived data (R2R data repository—see the "Data Availability" section). The seismic line starts from Chron M29 as distance zero for their stack and migration processes as well as sonobuoy locations. MCS, multichannel seismic.

anomalies (also see Supp. Info. S1 for the processes of this approach. See also Tominaga et al. [2008, 2015] and Tominaga & Sager [2010]).

For both inverse and forward sea surface models, we used a band-pass filter (2 km short-wavelength cutoff, 400-km long-wavelength cutoff) to focus on the crustal origin magnetic anomaly character (Supp. Info. S2; also see the Section 4.2). We used an ambient field inclination of 24.7° and a declination of 4.5° throughout modeling, calculated from the IGRF at the latitude and longitude of the survey location. We used a paleoinclination and paleodeclination of −7.96° and 5°, respectively, derived from the Pacific plate paleomagnetic apparent polar wander path of Larson and Sager (1992). Combined with these paleo declination and inclination estimations, the present day inclination and declination were also estimated from the midpoint of each survey line in order to correct for skewness (Petronotis & Gordon, 1989; Schouten & McCamy, 1972). We also used a constant thickness of 1 km for the magnetic source layer with the depth to its top defined by the topography of acoustic basement observed in the MCS data (Figure 2).

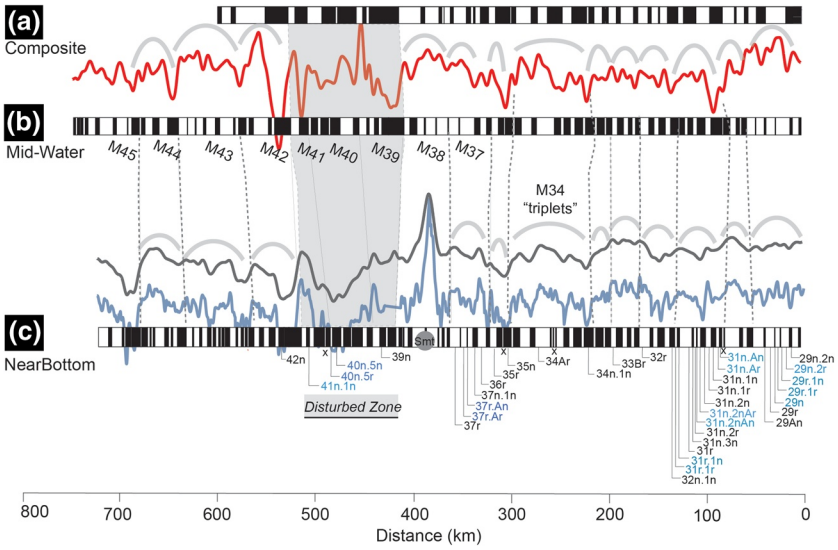

Figure 5. A comparison of the multiscale polarity block models of the Hawaiian M-sequence: (a) The composite sea surface level block model (Figure 4(a6)) and (b) the midwater level profile are the same as Figure 4(a) and 4(b) for comparison to (c) the near-bottom polarity block model. All profiles are projected onto a single, straight profile along the MCS line (heavy line in Figure 2(a)). Newly identified subchrons and cryptochrons are indicated in blue. The heavy black curve represents near-bottom level profile upward continued to midwater level and used as a basis for correlating the near-bottom and midwater profiles (same as the black solid curve in Figures 3(c)). Vertical dashed lines and gray band represent anomaly correlations, with the latter representing the Disturbed Zone discussed in the text. MCS, multichannel seismic.

Magnetic polarity block models for all three levels—sea surface, midwater, and near bottom—were constructed in the same manner as described above (Figures 4 and 5). Using the sea surface profiles, we identified the known M-series anomalies on each profile (Channell et al., 1995; Gradstein et al., 2012; Tominaga & Sager, 2010; Tominaga et al., 2015). A Hawaiian composite model was then built by averaging values of corresponding block boundary distances among four sea surface profiles (Figure 4(a6)).

4. Results

4.1. Anomaly Character and Multilevel Anomaly Correlations

Sea surface Line 26 (Figure 3) shows a well-defined magnetic anomaly sequence from M19 to at least M42 that closely correlates with the previously recognized magnetic anomalies of the Japanese lineation set (Tominaga et al., 2015). The other sea surface profiles mimic the anomaly character of Line 26 confirming the coherence of pre-M29 magnetic anomalies in the survey area (Figure 3).

The 125-km-wide spreading corridor, located between the Waghenaer and Waghenaer South fracture zones in pre-M18 crust, narrows to ∼25 km near 380 km along track, where two seamounts of the Marcus-Wake seamount chain bracket the profile (Figure 2). Sea surface Line 3 crossed directly over a small seamount in the middle of this bottleneck, while the near-bottom AUV line skirts the outermost edge of this seamount (Figure 2). The influence of seamount magnetism is apparent on Line 3 and also on the near-bottom AUV profile, but the effect is limited to only a few tens of kilometers along track at the beginning of M37 age crust (Figure 3).

Within a single spreading corridor, we expect some heterogeneity in mid-ocean ridge volcanism, even at fast spreading rates, which leads to variability in the recorded magnetic signal (e.g., Gee & Kent, 2007). The sea surface anomaly profiles are spread laterally across the surveyed corridor, which should average out volcanic heterogeneity to display the coherent anomaly pattern (Figures 2(a2) and 3). Anomaly M42 is a high-amplitude positive anomaly observed on all lines and marks the young edge of a broad positive that stretches back to M44. Anomalies M35–M38 create a positive ramp with M38 as the high point. On the young end of

the profiles, anomalies M29 and M30 create two small, similar positive anomalies and sometimes combine to a single positive hump. In between M30 and M34, the anomaly profile is generally flat.

When we upward continue the midwater profile (Figure 3(b)) to the sea surface, we observe long-wavelength anomaly features that exhibit the same character and pattern as those of the sea surface anomaly profiles (Figure 3(a) and 3(b)). This is also true for the upward-continued near-bottom AUV profile (Figure 3(b) and 3(c)), which mimics the midwater profile except for one amplified peak due to the seamount mentioned earlier (Figure 3(c)). The midwater profile is an important bridge for correlating long-wavelength chron "envelopes" between the sea surface and near-bottom AUV level magnetic anomalies. A good example of the magnetic anomaly internal consistency is the M34 "triplet" (220–300 km, Figure 3)—this distinctive sequence has three closely spaced, short-wavelength anomalies (Sager et al, 1998; Tivey et al., 2006). The near-bottom AUV profile reveals that each of the M34 peaks is composed of a broad anomaly with additional short-wavelength anomalies (Figure 5). These short-wavelength anomalies are ubiquitously observed within many of the chron "envelopes" and in the near-bottom AUV profile.

In contrast to this overall coherent pattern, we observe a consistent section of variable amplitude, difficult-to-correlate anomalies from Chron M39 to Chron M41. The location and extent of these difficult anomalies is similar to a sequence observed in the Japanese lineations which was noted as the Low Amplitude Zone or LAZ (Tominaga et al., 2015), the older bound of which is marked by Chron M42. While the Japanese LAZ is marked by very low amplitude anomalies, the Hawaiian Chron M39–M41 anomalies show highly variable amplitudes that are difficult to correlate between the sea surface, midwater, and near-bottom profiles and show no obvious correlation to the Japanese LAZ anomalies (Figure 3). Given this characteristic of the Hawaiian M39–M41 anomalies, we propose that this sequence be termed the Hawaiian Disturbed Zone (HDZ) to capture the high variability and lack of correlatability of these anomalies. The HDZ is preceded by a well-defined M42 anomaly similar to the Japanese sequence. Magnetostratigraphy of Jurassic sediments supports the existence of polarity reversals at the time of M42 (Llanos et al., 2019; Ogg et al., 2016), implying that this anomaly was caused by a magnetic reversal (Figure 3). We also note that despite its anomalous magnetic signature, the HDZ has a Layer 2A thickness of ~1.5 km, similar to the rest of the transect (Figure 2).

4.2. Polarity Block Models

Overall, the polarity block models built for each of the sea surface anomaly profiles exhibit similar locations for the major chrons between M29–M38 and M42–M43, with only minor variations in block widths and boundaries (Figures 4 and 5). When we compare the polarity block boundaries with the polarity block sequence from the pre-M29 Japanese lineation magnetic record (Tominaga et al., 2008) as well as the Geological Time Scale (Gradstein et al., 2012), we confirm that sea surface profiles 26, 974, 3, and 4 (profiles (a2)–(a5) in Figure 4) resolve the major anomalies between M29 and M43.

For all of the sea surface profiles, the locations of each polarity block boundary have standard deviations ranging nominally from 0.8 to 5.6 km, with a single exception of 10 km within M41, attesting to the lateral coherency of crustal recording by seafloor spreading within this flowline corridor. Among the four sea surface profile polarity block models, the most complete is sea surface Line 974 (Figure 4), which includes some of the subchrons that were previously only identified from the upward-continued near-bottom data in the Japanese sequence (Tominaga et al., 2008). We are able to locate the block boundary locations for Chrons M37 and M38 on other sea surface level profiles despite the signal disturbance by the nearby seamount (Figure 4). The largest scatter of polarity boundary locations is found within Chrons M39–M41, which are within the HDZ where correlation is unclear. We constructed a composite model (Figure 4 and Table 1) based on the four sea surface profiles following the protocol of determining "average" polarity boundary locations used by Tominaga and Sager (2010), that is, a chron or subchron is recognized if there are correlatable anomalies across more than two survey lines and the polarity boundaries are within the average of the modeled positions from each of the lines where it is recognized (e.g., Tominaga & Sager, 2010).

The block model based on the midwater anomaly profile is an important reference for assessing the locations of polarity block boundaries within both the sea surface and near-bottom AUV block models. Compared to the midwater and near-bottom block models of the Japanese lineation record (Tominaga et al., 2008), the

Table 1
Hawaiian GPTS Models

Sea surface level			Midwater level			Near-bottom level		
Chron	Distance	Age	Chron	Distance	Age	Chron	Distance	Age
M26r	0.00	**157.25**	M29n.2n	0.00	159.00	M29n.2n	0.00	159.11
M27n	2.28	157.29	M29r	24.40	159.43	M29n.2r	7.80	159.25
M27r	7.76	157.38	M29An	26.24	159.46	M29r.1n	9.50	159.28
M28n	19.80	157.59	M29Ar	44.28	*159.78*	M29r.1r	15.00	159.38
M28r	28.00	157.73	M30n	49.32	159.87	M29n[a]	15.80	159.39
M28An	33.60	157.83	M30r	51.48	159.91	M29r	23.90	159.54
M28Ar	45.00	158.03	M30An	55.04	159.97	M29An	26.50	159.59
M28Bn	52.16	158.15	M30Ar	61.20	160.08	M29Ar	37.20	*159.78*
M28Br	56.56	158.23	M31n.1n	80.80	160.42	M30n	42.90	159.88
M28Cn	63.76	158.35	M31n.1r	86.72	160.53	M30r	47.30	159.96
M28Dr	85.20	158.72	M31n.2n	94.96	160.67	M30An	50.70	160.02
M29n.2n	108.41	159.12	M31n.2r	99.24	160.75	M30Ar	65.70	160.29
M29r	128.93	159.48	M31n.3n	104.44	160.84	M31n.An	71.40	160.40
M29An	138.34	159.64	M31r	107.72	160.90	M31n.Ar	74.80	160.46
M29Ar	146.55	*159.78*	M32n.1n	122.04	161.15	M31n.1n	79.70	160.55
M30n	150.61	159.85	M32n.1r	127.40	161.25	M31n.1r	85.20	160.65
M30r	158.77	159.99	M32.2n	134.16	161.36	M31n.2n	90.50	160.74
M30An	160.58	160.03	M32n.2r	139.00	161.45	M31n.2nAr	93.90	160.80
M30Ar	172.87	160.24	M32n.3n	144.32	161.54	M31n.2nAn[a]	94.80	160.82
M31n.1n	186.01	160.47	M32r	153.12	161.70	M31n.2r	97.90	160.88
M31n.1r	199.82	160.70	M33n	158.00	161.79	M31n.3n	99.30	160.90
M31n.3n	212.62	160.93	M33r	161.40	161.85	M31r	111.80	161.13
M31r	218.31	161.02	M33An	165.28	161.91	M31r.1n[a]	113.30	161.15
M32n.1n	228.95	161.21	M33Ar	170.24	162.00	M31r.1r	116.90	161.22
M32n.1r	236.75	161.34	M33Bn	176.44	162.11	M32n.1n	122.10	161.31
M32.2n	238.23	161.37	M33Br	182.00	162.21	M32n.1r	127.40	161.41
M32n.2r	245.35	161.49	M33Cn.1n	187.72	162.31	M32.2n	134.20	161.53
M32n.3n	248.80	161.55	M33Cn.1r	189.80	162.35	M32n.2r	138.80	161.61
M32r	259.05	161.73	M33Cn.2n	197.36	162.48	M32n.3n	142.10	161.67
M33n	263.46	161.80	M33Cr	199.80	162.52	M32r	153.20	161.87
M33Ar	276.89	162.04	M34n.1n	209.24	162.69	M33n	158.00	161.96
M33Bn	281.20	162.11	M34n.1r	212.00	162.74	M33r	161.40	162.02
M33Br	289.15	162.25	M34n.2n	220.00	162.88	M33An	165.30	162.09
M33Cn.1n 295.59	162.36	M34n.2r	224.60	162.96	M33Ar	170.30	162.18	
M33Cn.1r 303.72	162.50	M34n3n	231.24	163.08	M33Bn	175.20	162.27	
M33Cn.2n 309.20	162.59	M34n.3r	234.44	163.13	M33Br	182.00	162.39	
M33Cr	311.36	162.63	M34An	241.04	163.25	M33Cn.1n	187.80	162.50
M34n.1n	326.55	162.89	M34Ar	259.28	163.57	M33Cn.1r[b]	189.80	162.53
M34n.3r	336.19	163.06	M34Bn.1n	264.24	163.66	M33Cn.2n	197.40	162.67
M34An	351.37	163.32	M34Bn.1r	274.80	163.84	M33Cr[b]	199.80	162.72
M34Ar	361.51	163.50	M34bn.2n	281.32	163.96	M34n.1n	209.30	162.89

Table 1
Continued

Sea surface level			Midwater level			Near-bottom level		
Chron	Distance	Age	Chron	Distance	Age	Chron	Distance	Age
M34Bn.1n 367.90	163.61	M34Br	283.52	164.00	M34n.1r	212.00	162.94	
M34Bn.1r 383.60	163.88	M35n	298.36	164.26	M34n.2n	220.00	163.08	
M34bn.2n 387.96	163.96	M35r	305.44	164.39	M34n.2r	224.60	163.16	
M34Br	389.40	163.98	M36n.1n	310.40	164.47	M34n3n	230.10	163.26
M35n	404.34	164.24	M36n.1r	317.00	164.59	M34n.3r	237.50	163.40
M35r	411.39	164.36	M37n.1n	322.80	164.69	M34An	243.80	163.51
M36n.1n	419.75	164.51	M37n.1r	337.80	164.96	M34Ar	259.30	163.79
M36n.1r	424.99	164.60	M37n.2n	338.84	164.97	M34Bn.1n	264.30	163.88
M36Cn	426.79	164.63	M37r	349.28	165.16	M34Bn.1r	274.80	164.07
M36Cr	429.54	164.67	M38n.1n	350.00	165.17	M34bn.2n	281.40	164.19
M37n.1n	434.15	164.75	M38n.1r	361.52	165.37	M34Br[b]	283.60	164.23
M37n.1r	447.13	164.98	M38n.2n	362.44	165.39	M35n	298.40	164.49
M37n.2n	450.26	165.03	M38n.2r	372.84	165.57	M35r	305.20	164.62
M37r	456.61	165.14	M38n.3n	374.32	165.60	M36n.1n	309.10	164.69
M38n.2n	461.96	165.24	M38n.3r	381.60	165.73	M36n.1r	317.90	164.85
M38n.2r	476.32	165.48	M38n.4n	388.96	165.86	M37n.1n	322.80	164.94
M38n.4n	480.36	165.55	M38n.4r	394.84	165.96	M37n.1r	328.10	165.03
M38n.4r	502.96	165.94	M38.5n	410.36	166.24	M37r.An[a]	328.80	165.04
M39n.1n	517.17	166.19	M38r	411.00	166.25	M37r.Ar	335.10	165.16
M39n.1r	534.04	166.48	M39n.1n	417.56	166.36	M37n.2n[b]	335.50	165.16
M39n.3n	539.62	166.58	M39n.1r	420.92	166.42	M37r	346.40	165.36
M39r	546.31	166.69	M39n.2n	425.16	166.50	M38n.1n	348.90	165.41
M40n.1n	565.49	167.02	M39n.2r	430.52	166.59	M38n.1r	352.00	165.46
M40n.1r	567.52	167.06	M39n.3n	433.04	166.64	M38n.2n[b]	354.10	165.50
M40n.3n	581.42	167.30	M39r	440.92	166.77	M38n.2r	357.40	165.56
M40r	596.34	167.56	M40n.1n	446.88	166.88	M38n.3n	358.50	165.58
M41n	608.84	167.77	M40n.1r	460.24	167.12	M38n.3r	370.00	165.79
M41r	615.75	167.89	M40n.2n	470.24	167.29	M38n.4n[a]	371.50	165.81
M42n.1n	639.28	**168.30**	M40n.2r	472.20	167.33	M38n.4r	384.80	166.05
M42n.1r	669.48	168.82	M40n.3n	480.12	167.47	M38.5n	388.80	166.13
M42n.2n	674.00	168.90	M40n.3r	483.24	167.52	M38r	392.80	166.20
M42n.2r	683.66	169.07	M40n.4n	489.84	167.64	M38r.4An[a]	393.90	166.22
M43n.1n	687.76	169.14	M40r	492.64	167.69	M38r.4Ar[a]	395.20	166.24
			M41n	502.04	167.85	M38n.Bn	398.00	166.29
			M41r	510.76	168.01	M38n.Br	401.00	166.35
			M42n.1n	527.44	**168.30**	M39n.1n	409.10	166.49
			M42n.1r	530.60	168.36	M39n.1r[b]	411.40	166.53
			M42n.2n	533.72	168.41	M39n.2n	417.40	166.64
			M42n.2r	549.00	168.68	M39n.2r	424.80	166.78
			M42n.3n	553.44	168.76	M40n.1n	430.20	166.87
			M42n.3r	556.52	168.81	M40n.1r	434.90	166.96

Table 1
Continued

Sea surface level			Midwater level			Near-bottom level		
Chron	Distance	Age	Chron	Distance	Age	Chron	Distance	Age
			M43n.1n	564.20	168.95	M40n.2n	445.30	167.15
			M43n.1r	567.64	169.01	M40n.2r[b]	446.80	167.17
			M43n.2n	569.40	169.04	M40n.3n	454.20	167.31
			M43n.2r	583.44	169.29	M40n.3r	456.80	167.35
			M43n.3n	588.04	169.37	M40n.4n	465.40	167.51
			M43n.3r	597.64	169.54	M40n.4r[a]	467.60	167.55
			M43n.4n	600.20	169.58	M40n.5n	472.00	167.63
			M43n.4r	607.60	169.71	M40r	473.40	167.65
			M43n.5n	608.64	169.73	M41n	484.00	167.85
			M43n.5r	616.28	169.87	M41n.1r	488.80	167.93
			M43n.6n	616.80	169.88	M41n.1n	491.80	167.99
			M43r	625.68	170.03	M41r	496.80	168.08
			M44n.1n	636.84	170.23	M42n.1n	509.20	*168.30*
			M44n.1r	645.56	170.38	M42n.Ar[a]	509.80	168.31
			M44n.2n	652.20	170.50	M42n.Bn	514.00	168.39
			M44n.2r	659.88	170.64	M42n.Br[a]	514.80	168.40
			M44n.3n	663.60	170.70	M42n.Cn	519.80	168.49
			M44n.3r	665.76	170.74	M42n.1r	523.40	168.56
						M42n.2n	529.60	168.67
						M42n.2r	535.10	168.77
						M42n.3n	539.50	168.85
						M42n.3r	544.90	168.94
						M43n.1n	550.30	169.04
						M43n.1nAr[a]	551.70	169.07
						M43n.1nBn[a]	553.80	169.11
						M43n.1nBr[a]	555.50	169.14
						M43n.1nCn	558.00	169.18
						M43n.1r	561.40	169.24
						M43n.2n[a]	563.20	169.27
						M43n.2r	569.50	169.39
						M43n.3n	574.10	169.47
						M43n.3nAr[a]	575.20	169.49
						M43n.3nBn	577.70	169.54
						M43n.3nBr[a]	579.00	169.56
						M43n.3nCn[a]	580.90	169.59
						M43n.3r	583.70	169.64
						M43n.4n	586.40	169.69
						M43n.4nAr[a]	588.40	169.73
						M43n.4nBn	592.20	169.80
						M43n.4r	597.80	169.90
						M43n.5n	600.20	169.94

Table 1
Continued

Sea surface level			Midwater level			Near-bottom level		
Chron	Distance	Age	Chron	Distance	Age	Chron	Distance	Age
						M43n.5r	606.00	170.05
						M43n.6n[a]	607.30	170.07
						M43r	613.60	170.18
						M44n.1n	622.60	170.35
						M44n.1r	627.20	170.43
						M44n.2n[a]	628.90	170.46
						M44n.2r	631.60	170.51
						M44n.3n	635.60	170.58
						M44n.3r	645.40	170.76
						M44.4n[a]	647.30	170.79
						M44.4r[a]	649.20	170.83
						M44.5n[a]	650.40	170.85
						M44.5r	652.90	170.89
						M44.6n	658.90	171.00
						M44.6r[a]	660.00	171.02

Note. Distance, location of the old end (base) of each chron in kilometers considering the old end of Chron M26r (sea surface) and M29Ar (midwater and near-bottom levels) as zero; M, M-series anomalies; bold letters, two age tie points used in this GPTS model. 157.3 and 168.3 Ma for the base of M29Ar and M42n.1n, respectively; italics letters, M29Ar age calculated based on the sea surface sequence with two age tie points; underlined letters, newly identified blocks.
[a]Newly identified blocks with less than 2.4 km width. [b]Blocks with less than 2.4 km widths.

midwater block model from this study resolves most of the short duration polarity blocks identified in the Japanese deep-tow data except for those within M36–M39 (Figure 4).

The AUV near-bottom polarity block model represents the highest resolution and possibly the most definitive record of all the possible crustal magnetic signals. This polarity block model initially resolved 26 additional polarity blocks compared to the midwater model, 6 of which are within M37 and M38 and 23 of which are within M43–M44 range (Figure 5 and Table 1). There are a total of 145 blocks within the 720 km profile. We named the new blocks temporarily by adding subchrons within the recognized major chron envelopes (Figure 5 and Table 1). A spectral analysis of the AUV near-bottom magnetic data (Supp. Info. S2) suggests that any blocks less than 2.4 km in length (i.e., a wavenumber of more than 0.4 km $F02D^1$) are within the "noise floor" of our measurements and so we recommend users to use this value as a cutoff for identifying the shortest polarity blocks.

The AUV near-bottom level polarity block model reveals a discrepancy within the M37 and M38 sequence with the Tominaga et al. (2008) record. Our AUV data block model now resolves six sets of normal and reverse polarity block pairs over the M37–M38 period, whereas the prior model showed fewer blocks (Tominaga et al., 2008). This discrepancy may be attributed to "polarity bias," that is, a polarity distribution favoring a normal or reverse state over a given time period, in the Japanese record. The distribution of the normal and reverse polarity blocks in our new model is consistent with the Callovian magnetostratigraphic record (e.g., Gipe, 2013; Ogg et al., 1992), which roughly corresponds to the period from M37 to the older half of M39 and is known to be a normal-polarity-dominated sequence. Thus, we suggest that the newly constructed record is a more realistic representation of the polarity distribution associated with this period of geomagnetic field behavior.

Finally, the AUV near-bottom level polarity block model displays many newly identified short-wavelength anomalies (ranging from 0.4 to 3.8 km), some of which are short in duration (Figures 3 and 5). Such short duration chrons have traditionally been termed "cryptochrons" (Cande & Kent, 1992b, 1995) and their origin has been the subject of debate (Lanci & Lowrie, 1997; Roberts & Lewin-Harris, 2000; Tominaga

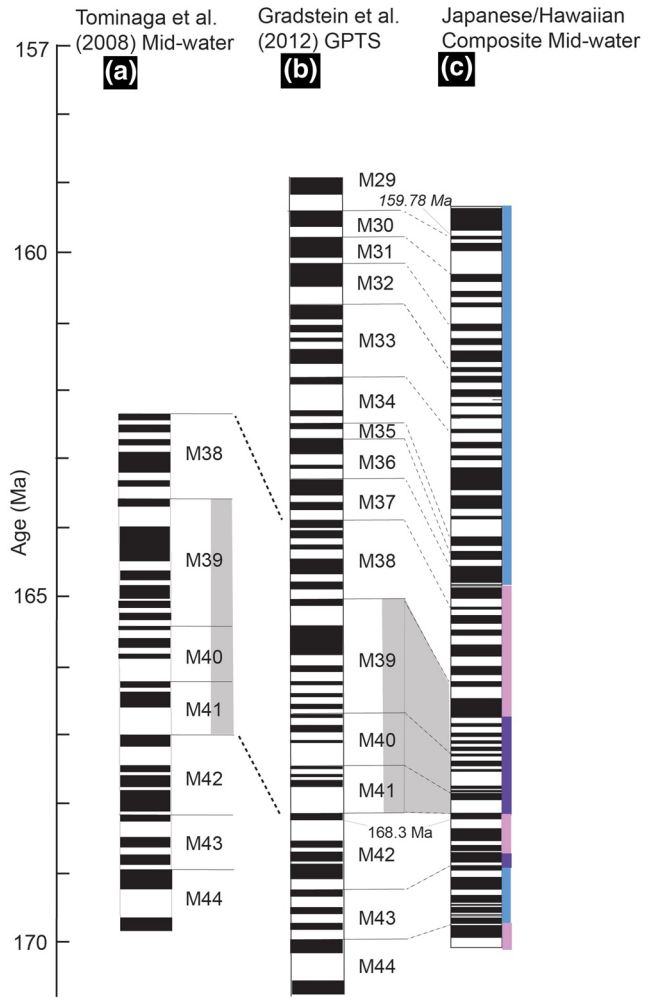

Figure 6. New GPTS model and comparison with previous versions. (a) A GPTS model (Tominaga et al., 2008) based on midwater level Japanese anomaly sequence; (b) GPTS 2012 midwater model with multiple age tie points (Gradstein et al., 2012); and (c) the new GPTS model from this study based on the compilation of Japanese midwater level upward-continued deep-tow data and the new Hawaiian midwater level data. The date of 159.78 Ma shown on the base of M29r is calculated from the sea surface level GPTS model using M26r and M42n.1n ages with a constant spreading rate assumption. Likewise, the date of 168.3 Ma at the base of M42n.1n is also calculated using the assumed constant spreading rate (see Section 4.3 in this study and Figures 5 .Figures 4 by Ogg et al. in Gradstein et al. [2012]). Polarity blocks accompanied with blue, pink, and purple bars indicate the compilation based on Hawaiian-only, the average of Japanese and Hawaiian, and Japanese-only data set, respectively (see the index on Table 2). Gray shades indicate the span of the LAZ and HDZ. GPTS, Geomagnetic Polarity Time Scale; LAZ, Low Amplitude Zone; HDZ, Hawaiian Disturbed Zone.

et al., 2008). Various origins have been suggested from actual short duration polarity reversals, to geomagnetic excursions, and paleointensity fluctuations (Bowles et al., 2003; Lanci & Lowrie, 1997; Roberts & Lewin-Harris, 2000). We consider the AUV near-bottom level polarity block model as an end-member possibility with the maximum number of reversals that may include both polarity reversals and paleointensity variations in the sequence (Table 1).

4.3. Defining Age Tie Points for the GPTS

The choice of age tie points to calibrate the Hawaiian lineation M-series GPTS block model is a challenge due to limited availability of absolute ages from ocean crust that can be directly correlated to marine magnetic anomalies. To build our M29–M42 sequence, we chose two radiometric age-based tie points from Geological Time Scale 2012 (Gradstein et al., 2012) that have a direct correlation between the measured rock and identified sea surface marine magnetic anomalies. These ages are: Chron M26r = 157.3 Ma and Chron M42n.1n = 168.3 Ma. (see Figures 5. Figures 4 by Ogg in Gradstein et al., 2012). The former is based on a radiometric age measured from crustal core samples with contemporaneous surface marine magnetic anomaly of M26n at ODP Site 765 and adjusted with various chronological information to take large uncertainties into account (±3.4 Ma, Ludden, 1992). The base of M26r aligns with the start of Kimmeridgian. The latter is also based on radiometric ages measured from crustal core samples with contemporaneous surface marine magnetic anomaly of M42r.4r at ODP Hole 801C and calculated and adjusted with various chronological information to take large uncertainties into account (±1.7 Ma, Koppers, Staudigel, & Duncan, 2003; Koppers, Staudigel, Pringle, et al., 2003) (see Table 5.5 by Ogg in Gradstein et al., 2012). The M42n.1n aligns with the start of Bathonian.

We first apply linear interpolation and extrapolation for the sea surface level magnetic polarity block model to obtain an age of each polarity boundary, assuming a constant crustal spreading rate. Using these age tie points, we extrapolate our new GPTS model to the base of Chron M44r resulting in a proposed age of 170 Ma (Figure 6 and Table 1). For calculating the spreading rates, we used a distance of 648 km for the interval between M26r and M42n.1n (Table 1) that yields a half-spreading rate of 56.7 km/Myr. The midwater and near-bottom level sequences start from Chron M29. With a new GPTS model for the surface level magnetic polarity block model established, we then take the interpolated age of Chron M29r (=159.78 Ma) from this model and use it as an age tie point for both the midwater and near-bottom level GPTS models (Table 1).

With the new Hawaiian record, we can construct a composite Japanese–Hawaiian GPTS from M29 to M44. To maintain consistency with the use of the previously published midwater polarity sequence data in constructing GPTS 2012 (Gradstein et al., 2012), we define our midwater level block model as our primary polarity block model (e.g., Sager et al., 1998; Tominaga et al., 2008). To build the composite GPTS model, we used the midwater level Hawaiian block model and the midwater level Japanese block model (i.e., upward-continued deep-tow block model) (Tominaga et al., 2008) (Figure 6 and Table 2). Some parts of the composite model are constructed in a piece-meal compilation manner because not all of the chrons identified in the Japanese upward-continued midwater data are found in the Hawaiian midwater data. As a result, this composite model consists of the following sections: (1) polarity boundary locations for M29–M37n.1r are built only with Hawaiian data from this

Table 2
Japanese–Hawaiian Midwater Level Composite Geomagnetic Polarity Reversal Time Scale Model

Chron	Distance	Age	Index
M29n.2n	0.00	159.06	H
M29r	24.40	159.46	H
M29An	26.24	159.49	H
M29Ar	44.28	**159.78**	H
M30n	49.32	159.86	H
M30r	51.48	159.90	H
M30An	55.04	159.95	H
M30Ar	61.20	160.05	H
M31n.1n	80.80	160.37	H
M31n.1r	86.72	160.47	H
M31n.2n	94.96	160.60	H
M31n.2r	99.24	160.67	H
M31n.3n	104.44	160.75	H
M31r	107.72	160.80	H
M32n.1n	122.04	161.04	H
M32n.1r	127.40	161.12	H
M32.2n	134.16	161.23	H
M32n.2r	139.00	161.31	H
M32n.3n	144.32	161.40	H
M32r	153.12	161.54	H
M33n	158.00	161.62	H
M33r	161.40	161.67	H
M33An	165.28	161.73	H
M33Ar	170.24	161.81	H
M33Bn	176.44	161.91	H
M33Br	182.00	162.00	H
M33Cn.1n	187.72	162.10	H
M33Cn.1r	189.80	162.13	H
M33Cn.2n	197.36	162.25	H
M33Cr	199.80	162.29	H
M34n.1n	209.24	162.44	H
M34n.1r	212.00	162.49	H
M34n.2n	220.00	162.62	H
M34n.2r	224.60	162.69	H
M34n3n	231.24	162.80	H
M34n.3r	234.44	162.85	H
M34An	241.04	162.96	H
M34Ar	259.28	163.25	H
M34Bn.1n	264.24	163.33	H
M34Bn.1r	274.80	163.50	H
M34bn.2n	281.32	163.61	H
M34Br	283.52	163.64	H

study; (2) polarity boundary locations for M37n.2n–M39n.1, M42n.1n–M42n.3r, M43n.1n–M43n.3r, and M44 are built by taking the average of each of the polarity boundary locations (cf., Cande & Kent, 1992a, 1992b) between Hawaiian data from this study and Japanese data from Table 2 in Tominaga et al. (2008). We scaled the distance of Japanese lineation data over this period to that of Hawaiian; and (3) polarity boundary locations for M39n.1r–M41r and M42n-r are built only with scaled Japanese data (Table 2 in Tominaga et al., 2008).

5. Discussion

We model a revised GPTS (Figure 6) for the Mid to Late Jurassic period based on newly acquired multiscale magnetic data from the Pacific Hawaiian magnetic lineation sequence and correlate it with the previous Japanese magnetic lineation record (Tominaga et al., 2008). We present the Hawaiian-Japanese compilation GPTS model using two age tie points from Gradstein et al. (2012) assuming a constant spreading rate. To verify that the magnetic anomaly sequence represents geomagnetic field variations, we first discuss the potential impact of late-stage volcanic overprint on the Pacific Jurassic record. We then discuss the broad scale implications of this new GPTS (Figure 6) in terms of long-term geomagnetic field behavior, polarity reversal history, and the origin of the M39–M41 HDZ. Finally, we discuss implications of the revised spreading rates for the Mid Jurassic to Early Cretaceous Pacific.

5.1. Evaluating the Impact of Cretaceous Volcanic Overprint

While the crust of the western Pacific was formed by Jurassic mid-ocean ridge seafloor spreading, broad areas of the Pacific plate were subjected to Cretaceous volcanism in the form of numerous seamounts and large igneous provinces (Larson, 1991; Stadler & Tominaga, 2015). Most of the large volcanic features are documented by satellite altimetry data, but it is common to observe small seafloor volcanic features using ship multibeam sonar and high-resolution MCS data (e.g., D. K. Smith & Jordan, 1987, 1988; Stadler & Tominaga, 2015). Furthermore, in addition to extrusive volcanics apparent at the seafloor, seismic profiles provide evidence of subseafloor volcanic features, such as volcanic sills within sediments and upper crust (Abrams et al., 1992; Feng, 2016; Kaneda et al., 2010; Lancelot, Larson, & Fisher, 1990; Lancelot, Larson, & Shipboard Scientific Party, 1990; Mochizuki et al., 2005; Schlanger & Moberly, 1986; Stadler & Tominaga, 2015; Tominaga et al., 2008).

To assess the impact of such volcanism as a potential overprint of the original Jurassic magnetic remanence, it is instructive to both map such features and model the potential impact on the geomagnetic record. The MCS reflection profile and seismic refraction crustal model, colocated with these new magnetic data (Figures 1 and 2), document volcanic features within the crustal and sediment section of the transect (Feng et al., 2015). Based on the combination of MCS and velocity models, the sedimentary cover varies in thickness from 0.1 to 1.1 km with a median value of 0.58 km along the survey transect (Figures 2(b) and 2(c)). Satellite-derived bathymetry, multibeam mapping, and MCS profiles all confirm that the surveyed spreading corridor is free of fracture zones and has a smooth, sediment-blanketed oceanic crust over typical fast spreading

Table 2
Continued

Chron	Distance	Age	Index
M35n	298.36	163.88	H
M35r	305.44	164.00	H
M36n.1n	310.40	164.08	H
M36n.1r	317.00	164.19	H
M37n.1n	322.80	164.28	H
M37n.1r	337.80	164.52	H
M37n.2n	338.84	164.54	A
M37r	349.28	164.71	A
M38n.1n	356.59	164.82	A
M38n1r	358.24	164.85	A
M38n.2n	363.55	164.94	A
M38n2r	369.98	165.04	A
M38n.3n	375.53	165.13	A
M38n3r	379.85	165.20	A
M38n.4n	387.90	165.33	A
M38n4r	397.20	165.48	A
M38.5n	405.68	165.62	A
M38r	412.55	165.73	A
M39n.1n	418.34	165.82	A
M39n1r	422.32	165.89	SJ
M39n.2n	432.37	166.05	SJ
M39n2r	447.83	166.30	SJ
M39n.3n	453.07	166.38	SJ
M39n3r	455.45	166.42	SJ
M39n4n	461.00	166.51	SJ
M39n4r	463.76	166.56	SJ
M39n5n	467.36	166.61	SJ
M39n5r	469.52	166.65	SJ
M39n	472.58	166.70	SJ
M39r	475.43	166.74	SJ
M40n.1n	478.30	166.79	SJ
M40n1r	479.96	166.82	SJ
M40n.2n	484.20	166.89	SJ
M40n2r	488.09	166.95	SJ
M40n.3n	491.12	167.00	SJ
M40r	492.63	167.02	SJ
M41n1n	504.93	167.22	SJ
M41n1r	506.93	167.25	SJ
M41n2n	508.53	167.28	SJ
M41n2r	509.75	167.30	SJ
M41n	511.02	167.32	SJ
M41r	516.18	167.40	SJ
M42n1n	527.44	**168.30**	A

basement topography (Figures 1(a), 2(b) and 2(c)). The MCS data show areas of volcanic intrusion within the sediment section in the form of volcanic sills and flows, with widths varying from a kilometer to a few kilometers and a nominal thickness of ~100 m based on our velocity model (Figure 2(b)) (Feng, 2016; Feng et al., 2015); although they are prevalent only in the 0–110 km section of the profile (e.g., Feng, 2016; Feng et al., 2015) (Figure 2(b)). Seamounts are located at 450, 700, and 750 km along track. From north to south, the seismic Layer 2 crustal velocity model shows a constant thickness of 0.8–1.0 km in the 0–350 km portion of the profile, which then thickens to 1.5–1.6 km between 350 and 800 km in the Marcus-Wake seamount province (Figures 1 and 2). Using the observed dimensions of volcanic sills varying from 2 to 4.8 km in width (median 2.2 km) and ~500 m beneath the seafloor within the sediment sequence (e.g., Feng, 2016; Feng et al., 2015), we calculate the predicted magnetic anomaly using polygon modeling (Talwani & Heirtzler, 1964) (Supp. Info. S1). Results show that such volcanic sills produce anomalies with amplitudes of only a few nanoteslas at the sea surface (Supp. Info. S3), implying only minor perturbations to anomaly profiles.

Crustal thickening, that is, apparent magnetic source thickening, along the profile between 350 and 800 km would generally suggest a concomitant increase in anomaly amplitude (Figures 2(b), 2(c), and 3); however, the effect is small and it is long wavelength and smooth, so it does not affect polarity interpretations. To verify this, we forward modeled the variable source thickness to compare with the observed sea surface anomalies (Supp. Info. S4). We note that while changes in thickness do impact the overall amplitude slightly (12–23 nT), it does not change the location of polarity boundaries (Supp. Info. S4). This exercise confirms that, even with considering a deeper magnetic source, for example, Layer 3, the decrease in magnetic field caused by distance to the source; and hence, the upper surface of the source layer, such as Layer 2A, gives the greatest effect.

Moreover, as shown earlier (Figure 3(a)) (Tominaga et al., 2015), anomaly amplitude continuously decreases back in time until M42. This inverse correlation confirms that crustal thickening does not change the nature of magnetic anomalies in this part of the JQZ in the broad picture, including the short-wavelength wiggles identified within our near-bottom AUV profiles. We propose that crustal structure or late-stage volcanism has little effect on the overall Hawaiian magnetic polarity sequence except for the area identified as the HDZ.

5.2. Long-Term Variations in Geomagnetic Field Amplitude: Implications for the Mesozoic Dipole Low

The new Hawaiian magnetic anomaly record corroborates prior deep-tow magnetic data studies from the Japanese magnetic lineations (Sager et al., 1998; Tivey et al., 2006; Tominaga et al., 2008) of a long-term decrease in magnetic anomaly amplitude into the JQZ back in time, at least until the M38–M41 period (Figure 4(a1)) (Tominaga et al., 2015). Prior to this time, anomaly amplitudes appear to have higher values from M42 back to M44 (Figure 4(a1)) (Tominaga et al., 2015). This long-term decrease in anomaly amplitude into the JQZ based on marine magnetic anomalies was first noted by Cande et al. (1978) up to M25 and was subsequently extended by later surveys (Handschumacher et al., 1988;

Table 2
Continued

Chron	Distance	Age	Index
M42n1r	531.80	168.37	A
M42n2n	539.54	168.50	A
M42n2r	549.09	168.65	A
M42n3n	552.93	168.71	A
M42n3r	557.10	168.78	A
M42n	558.57	168.80	J
M42r	568.91	168.97	J
M43n.1n	569.51	168.98	A
M43n.1r	572.40	169.03	A
M43n.2n	578.12	169.12	A
M43n.2r	587.56	169.27	A
M43n.3n	592.46	169.35	A
M43n.3r	599.59	169.47	A
M43n.4n	600.20	169.48	H
M43n.4r	607.60	169.59	H
M43n.5n	608.64	169.61	H
M43n.5r	616.28	169.74	H
M43n.6n	616.80	169.74	H
M43r	625.68	169.89	H
M44n1n	633.75	170.02	A
M44n1r	646.51	170.22	A

Note. Distance, location of the old end of each chron, considering the old end of Chron M29n.2n as zero; M, M-series anomalies; bold letters, two age tie points used in this GPTS model. 157.3 and 168.3 Ma for the base of M29Ar and M42n.1n, respectively; Index H, Hawaiian lineation data only; A, averaged Hawaiian and Japanese lineation data; SJ, Scaled Japanese data (see Section 4.3); J, Japanese lineation data only.

Sager et al., 1998; Tominaga et al., 2008). McElhinny and Larson (2003) suggested that changes in anomaly amplitude over time could be used as a proxy of paleointensity variation, such that this decrease in marine magnetic anomaly amplitude reflects a long-term change in geomagnetic field intensity and corresponds to a period called the "Mesozoic Dipole Low" where field intensity was anomalously weak (Biggin & Thomas, 2003; Prévot et al., 1990; Thomas & Biggin, 2003).

This observation of weak field intensity within the JQZ period is supported by paleointensity studies on a few rock samples (inset of Figure 7) (Biggin et al., 2008; Ingham et al., 2014; Tauxe et al., 2013). A recent rock magnetic study with strict sample measurement criteria indicates that the "Mesozoic Dipole Low" may have been ~50 Myr in duration (Tauxe et al., 2013) with an average dipole moment of $28.7 \pm 14 \times 10^{21}$ A m^2, well below the long-term value of 42×10^{21} A m^2. Furthermore, submarine basaltic glass data from ODP Hole 801C (Figures 7 in Tauxe et al., 2013) indicate higher axial dipole moments, which coincides with M42, whereas basaltic glass data from younger crust (Figure 7 in Tauxe et al., 2013) show generally lower values (Figure 7). This higher intensity at M42 and earlier corresponds with our observations of greater anomaly amplitudes for the M44–M42 sequence. Following the same rationale as McElhinny and Larson (2003), we interpret the Hawaiian and Japanese data as indicating normal field intensity between M44 and M42 followed by the rapid onset of weak field intensity into the Mesozoic Dipole Low followed by a gradual increase in field intensity toward Cretaceous time. This pattern in anomaly amplitudes appears to be consistent with sparsely available rock magnetic data over the range of Jurassic–Early Cretaceous time period (Figure 7).

5.3. High Reversal Rates During Mesozoic Dipole Low

Our new composite Mid Jurassic polarity block model provides important insight on, and implications for, estimates of polarity reversal rates, which can be a basis for understanding the kyr-to-Myr time scale behavior of Earth's geomagnetic field (e.g., Constable, 2003; Kulakov et al., 2019; Lowrie & Kent, 2004; McFadden & Merrill, 1993; Smirnov et al., 2017). Such models, in turn, provide important insight on the nature of the geodynamo (e.g., Biggin et al., 2015; Constable, 2003; Courtillot & Besse, 1987; Hounslow et al., 2018; Kulakov et al., 2019; Larson & Olson, 1991; Olson & Amit, 2015; Takahashi et al., 2005; Tarduno & Cottrell, 2005; Tarduno et al., 2006). For this study, however, the paucity of contemporaneous, continuous, sedimentary, or volcanic flow sequences with high-resolution geomagnetic records limits our interpretation of a definitive origin for these features. Even when high-resolution sedimentary (Bowers et al., 2001; Bowles et al., 2003) and volcanic flow magnetostratigraphy sequences are available (Knudsen et al., 2009; Otofuji et al., 2013), ambiguity remains because of the lack of detailed age control. We can however investigate end-member representations of geomagnetic field behavior based on our new GPTS model.

By applying a 4 Myr moving window average to the new GPTS model (Figure 6 and Table 1), we estimate the median polarity reversal rate for the surface, midwater, and near-bottom level GPTS models to be 11, 19, and 22 rev/Myr, respectively, for the period between M29 and M44. The 11/Myr rate is higher but close to previous estimates of 8/Myr (Tominaga et al., 2008) and 7/Myr (Tivey et al., 2006) for the same period. The reversal rate of 19/Myr based on our "reference" midwater level GPTS model is much higher than the midwater level estimates from the Japanese lineation set midwater level data of 8 rev/Myr (Tominaga et al., 2008). We propose that the midwater level reversal rate from this study is more representative because it has a better signal to noise than our previous estimates. The low reversal rates in the midwater level profile from the

Tominaga et al. (2008) study were due mainly to the ∼2 km upward continuation filtering of the deep-tow data to construct a midwater level model, whereas in this study the midwater level data needed only minimal upward continuation of less than a few hundred meters from the original data acquisition level.

The estimate from the AUV near-bottom GPTS provides the highest rate of 22/Myr, which is consistent with the estimated rate of 26/Myr from the near-bottom level GPTS in the Japanese lineation set (Tominaga et al., 2008). Recent geomagnetic studies suggest that even the highest end of the estimated reversal rate of 26/Myr is not an anomalous scenario. McFadden and Merrill (1993) suggested that the average reversal event requires ∼5 kyr in transition from one polarity to the other. Assuming this interval on both sides of a polarity period, our inferred rate of 26/Myr implies polarity periods of ∼33 kyr length. This polarity duration is plausible based on previously observed short duration polarities in Earth's geomagnetic field history. For example, it is only 5 kyr shorter that the shortest, best documented, and dated reversal event within the Réunion event (e.g., Baksi & Hoffman, 2000) or subchron (e.g., Channell et al., 2003), that is, the globally identified Feni subchron of ∼38 kyr, that is found in both sediments and volcanics, and spans 2.153–2.115 Ma with $^{40}Ar/^{39}Ar$ and U–Pb dating (Baksi & Hoffman, 2000; Channell et al., 2020; Singer et al., 2014). Furthermore, an extremely short duration Chron E23r has been documented during the Late Triassic (Deenen et al., 2011; Kent & Olsen, 1999, 2008; Kent et al., 2017). A number of different dating approaches yielded 11–28 kyr durations for this particular chron, suggesting that polarity reversal events in the order of a few tens of kiloyears are not anomalous. Given these well-documented frequency examples, reversal rates estimated from our new AUV near-bottom level GPTS model suggest that even the highest end-member on the reversal rate spectrum is possible.

Superimposed on the reversal rate history is the role of paleofield intensity. Clearly, many of the shorter events of the new GPTS could also be paleointensity fluctuations rather than polarity reversals (Bowers et al., 2001; Bowles et al., 2003; Roberts & Lewin-Harris, 2000). Without well-established magnetostratigraphic and age-dated rock magnetic estimates of polarity and field intensity for the Middle Jurassic to Early Cretaceous, it is difficult to resolve the difference between polarity and paleointensity variations. There have been efforts to link reversal rate and paleointensity in the research literature. For example, recent work suggests that superchrons like the CNS or Permo-Carboniferous Reversed Superchron—periods of low reversal activity—have relatively high field intensity (Tarduno & Cottrell, 2005; Tarduno et al., 2001; Tauxe et al., 2013) and by inference that rapid reversals are associated with low field intensity (e.g., Bono et al., 2019). Recent work by Kulakov et al. (2019) presented the idea of Jurassic Hyper Activity Period for 155–170 Ma, during which the inverse correlation between the geomagnetic paleointensity and reversal frequency was observed (e.g., Figures 3, Figures 5, Figures 6, Figures 8, and Figures 10 in Kulakov et al., 2019). Geodynamo models appear to support this view (Buffet, 2000; Glatzmaier, 2002; Glatzmaier & Roberts, 1995; Olson et al., 1999, 2013). The JQZ period, as shown by our newly defined GPTS, proposes both rapid reversals and weak field intensity based on the anomaly amplitude envelope, which is consistent with this paradigm.

Directional stability of Earth's geomagnetic field is also thought to have an inverse relationship with reversal rates (Constable, 2003; Cronin et al., 2001; McFadden et al., 1991), suggesting that there may be little directional stability of the geomagnetic field if the field reverses polarity at such high rates. We note, however, that, except for the Hawaiian HDZ and Japanese LAZ zones, there is coherence between the Japanese and Hawaiian magnetic anomaly sequences down to the shortest wavelengths in these records (Figure 3 and Table 1). The coherency between lineations ∼700 km apart using the locations of Chron M42 implies that the crustal magnetic signals represent a geomagnetic field that is consistent over at least this spatial scale and potentially extrapolated over multiple lineation sequences within both Hawaiian and Japanese lineation sets.

5.4. The Origin of the Hawaiian Disturbed Zone

The new Hawaiian marine magnetic anomaly sequence displays correlatability from M29 to M38 and again between the distinctive anomaly M42 and the end of the record at M44 (Figure 3). Between these correlatable sequences is an uncorrelatable sequence bounded by M39 and M41. This time period falls within the early phase of the Mesozoic Dipole Low period as discussed above. This time period was previously

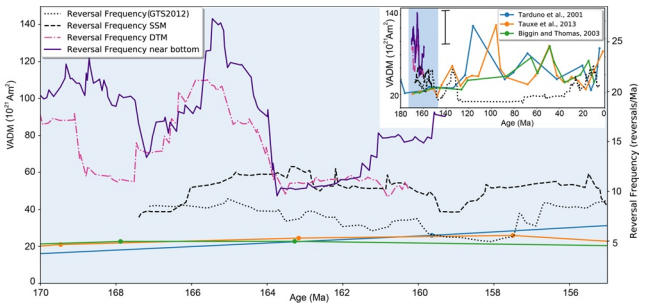

Figure 7. Comparison between the virtual axial dipole moment (VADM) intensity of the geomagnetic field and reversal rates over time based on the GPTS from this study. The VADM models are based on rock magnetic experiments made by for example, Tarduno et al. (2001) and Tauxe et al. (2013) and rock magnetic data based estimates made by Biggin and Thomas (2003). Upper right corner inset shows VADM estimates from 0 to 180 Ma; the vertical band corresponds to the main figure. SSM, sea surface magnetic profile; DTM, deep-tow/midwater level magnetic profile; near bottom, AUV Sentry magnetic profile. GPTS, Geomagnetic Polarity Time Scale; AUV, Autonomous Underwater Vehicle.

identified in the Japanese lineation sequence as the LAZ because of the dominance of low amplitude, uncorrelatable wiggles, even in deep-tow data (Tivey et al., 2006; Tominaga et al., 2008, 2015). However, our study shows that contemporaneous crust in the Hawaiian lineation sequence contains much greater variability in anomaly amplitudes and spacing, yielding a chaotic anomaly character. This lack of correlation extends throughout the various magnetic data sets from the sea surface through to the midwater and near-bottom AUV records—all become difficult to correlate within this period (Figure 3). This suggests that the uncorrelatability is not due to the differences in signal-to-noise ratios among the multiscale data. As mentioned earlier, a period of weak geomagnetic field intensity, that is, the Mesozoic Dipole Low, appears to reach its minimum value during the M39–M41 period in the HDZ, before the field intensity apparently rebounds in strength at Chron M42 and in older crust, an observation that is also mirrored in the Japanese LAZ sequence—both show Chron M42 as the last anomaly prior to the onset of these disturbed and difficult-to-correlate periods and potentially the beginning of the Mesozoic Dipole Low.

The HDZ sequence also corresponds to the influence of the Marcus-Wake seamount chain (Figure 8). In the Hawaiian lineations, Chron M42 and older anomalies are clearly identifiable on the magnetic profiles despite still being within the Marcus-Wake seamount region (Figures 3 and 8). In contrast, for the Japanese LAZ sequence, weaker anomalies can be more readily observed because the crust has less impact from the seamount chain (Figure 8). Given these observations, we propose that late-stage volcanism contamination in the form of the Cretaceous-aged Marcus-Wake seamount chain has the greatest effect on Jurassic-aged crust formed during the period of time when the field was weakest, which corresponds with the HDZ and LAZ portions of the Hawaiian and Japanese sequences, respectively. The effect is more obvious in the Hawaiian sequence compared to the Japanese sequence given the greater impact of the seamount terrain in the Hawaiian profile. Tominaga et al. (2008) discussed several reasons why the Japanese LAZ was marked by uncorrelatable, low amplitude anomalies and concluded that that low field intensity and rapid reversals could potentially lead to a reduction of anomaly amplitudes (see Figure 12 in Tominaga et al., 2008). The HDZ sequence appears to offer no further insight into this period of field behavior because of the crustal contamination overprint from the Marcus-Wake seamount chain that likely masks weak crustal anomalies.

5.5. Spreading Rate Estimates and Implications for Pacific Plate Evolution

The new GPTS (Figure 6) necessarily must make assumptions about the spreading rate for the Hawaiian lineation set for Pre-M29 crust. Half-spreading rates for the M0–M29 "M-series" of the Hawaiian lineation set have been previously reported as 30–50 km/Myr, depending on age tie points (Channell et al., 1995; Larson & Hilde, 1975). Malinverno et al. (2012) used a comprehensive post-M29 M-series data set from Tominaga and Sager (2010) and calculated the best common spreading rates for both Japanese and Hawaiian M-series magnetic lineations, yielding approximately 57 km/Myr.

We have three age dates with which to tie the Hawaiian lineation sequence and calculate interval spreading rates. While the M26n (155.3 ± 3.4 Ma; Ludden, 1992) and M42n (167.4 ± 1.7 Ma; Koppers, Staudigel, & Duncan, 2003) tie points, and the adoption of Gradstein et al. (2012)'s adjusted ages of M26r = 157.3 Ma, and M42n.1n = 158.3 Ma, are generally accepted, the starting M0r age date for the M-series is the subject of some debate (Malinverno et al., 2012; Olierook et al., 2019; Tominaga & Sager, 2010; Y. Zhang et al., 2019). The current time scale uses 125 Ma (Gradstein et al., 2012) as the age for M0r, however, more recent work suggests a younger age between 123.8 and 121.8 Ma (Olierook et al., 2019) with Y. Zhang et al. (2019), He et al. (2008) suggesting 121.2 Ma, and Erba et al. (2015) suggesting 121 Ma.

Using the proposed end-member 121 Ma age (Erba et al., 2015) and the 125 Ma estimate for M0r in the current time scale (Gradstein et al., 2012) with an anchored value of 157.3 Ma for the M26n age, we can calcu-

late two possible spreading rates for the M0r–M26n Hawaiian lineation sequence over its profile distance of 1837 km (Tominaga & Sager, 2010). This calculation gives 50.6 and 60 km/Myr using the base of M0r as 121 or 125 Ma, respectively. These rates are at the higher end of the range of the earlier estimates (e.g., Channell et al., 1995; Larson & Hilde, 1975; Nakanishi et al., 1989) but consistent with the recent estimation using Malinverno et al. (2012) and Tominaga and Sager (2010). The half-spreading rate of 56.7 km/Myr, which is almost the same as the overall estimate for the younger portion of the Hawaiian sequence, suggests that the seafloor spreading that formed the Hawaiian lineation sequence has been more or less steady throughout the M-series period. In contrast, the half-spreading rate for M29–M42 in the Japanese lineation set is faster at 67 km/Myr (Tominaga et al., 2008) but then decreases by 15% to 57 km/Myr in crust younger than M29, more in line with the Hawaiian spreading rates. Magnetic anomaly studies near Shatsky Rise imply that the Pacific-Izanagi ridge, which recorded the Japanese lineations, underwent a Late Jurassic reorganization (Nakanishi et al., 1998; Sager et al., 1998) that can explain this difference in rates.

6. Conclusions

Based on new multiscale magnetic data from the Pacific Hawaiian magnetic lineation sequence including sea surface, midwater, and AUV near-bottom magnetic profiles, we have modeled a new GPTS (Figure 6) for the Mid to Late Jurassic. This GPTS has been correlated with the previous high-resolution Japanese magnetic lineation record to provide a comprehensive record based on two spreading center magnetic polarity records. This model leads to the following conclusions:

(i) The new Hawaiian magnetic reversal record correlates closely with the previous Japanese magnetic reversal record supporting the interpretation that it is a faithful representation of geomagnetic field behavior for the Mid to Late Jurassic.

(ii) The Hawaiian and Japanese high-resolution magnetic anomaly data, independent of the rock magnetic record, suggest the rapid onset of a weak magnetic field following M42 is the beginning of the Mesozoic Dipole Low that reaches its lowest value of axial dipole moment between M41 and M39 but then begins a gradational recovery in strength into the Cenozoic.

(iii) The new GPTS suggests reversal rates ranging between 11, 19, and 22 (rev/Myr) based on the sea surface, midwater, and near-bottom resolution profiles, respectively. The highest end-member on the reversal rate spectrum is comparable with previous estimates of 26 rev/Myr from the Japanese lineation near-bottom data. Furthermore, we find a correlation between rapid reversal rate and low field intensity. While we cannot unambiguously separate polarity reversals from intensity fluctuations, we find a significant level of coherency between these short-wavelength anomalies for both the Japanese and Hawaiian lineation magnetic anomaly sequences, which suggests the existence of spatially coherent and directional stable field during this period of rapid field change.

(iv) Similar spreading rates were obtained independently in two intervals, M42–M26 and M26–M0 in the Hawaiian sequence with a steady half-spreading rate of about 57 km/Myr, suggesting that spreading rates remained approximately constant in the Hawaiian lineation throughout this time period. This is slightly slower than the Japanese sequence for M42 through M29, which has an initial half-spreading rate of about 67 km/Myr; but then, the spreading rates slow down to the same 57 km/Myr for crust younger than M29 probably due to contemporaneous tectonic events in the western Pacific.

(iv) The western Jurassic ocean crust Pacific has a Cretaceous volcanic overprint that includes seamounts and subseafloor volcanic features such as volcanic sills within the sediments and upper crust as well as an overall increase in the thickness of the seismic crust. Despite this clear late-stage volcanic overprint, the influence of these volcanics on the Hawaiian magnetic anomaly sequence appears to be limited. However, we can identify a zone of difficult-to-correlate anomalies, which we term the HDZ, which is identical in age with a similar LAZ zone in the Japanese lineations. We suggest that the geomagnetic field intensity during this period was so weak that late-stage Cretaceous volcanism in the Hawaiian sequence has a greater influence in distorting weakly recorded Jurassic geomagnetic signals than in the Japanese sequence. The HDZ, bounded by M39–M41 isochrons, may in fact represent the core of what is more commonly known as the JQZ crust

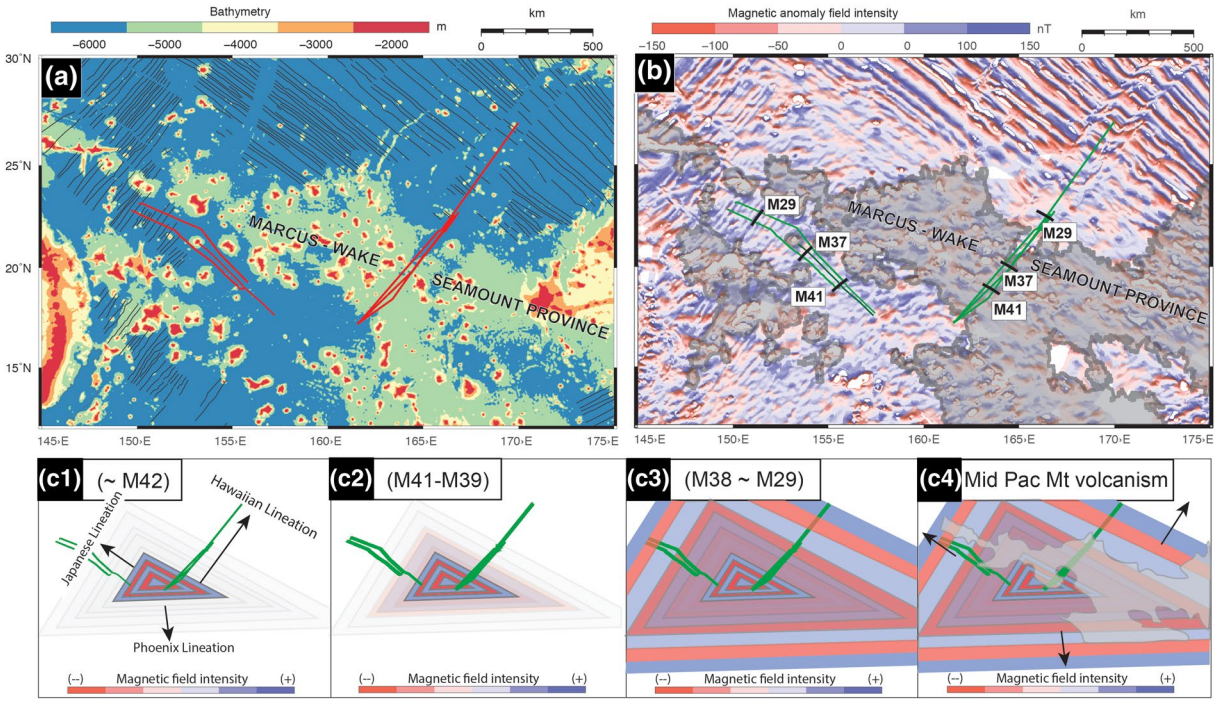

Figure 8. Satellite based bathymetry (a) and EMAG2v3 sea surface level magnetic anomaly (b) maps of the western Pacific region where the M-sequence seafloor spreading anomalies emerge as Japanese and Hawaiian sequences (cf., Figure 1). The magnetic anomaly map shows distinct changes in anomaly amplitudes for pre-M29 anomalies, which Marcus-Wake Seamount Province (gray shaded) overlaps in the Hawaiian lineations. Satellite bathymetry is v. 19.1 (Sandwell & Smith, 1997); satellite magnetic anomalies are the EMAG2v3 compilation (Meyer et al., 2017). (c1–c4) Sketch of relation between the evolution of the early Pacific plate and contemporaneous paleogeomagnetic field strengths represented by the gradation of color (blue = positive and red = negative polarities of the field). The gray shading in (c4) indicates the Mid-Pacific mountain volcanism that affect the magnetic signals particularly those acquired during the period of the lowest dipole field.

Data Availability Statement

Data used in this study are available through Rolling Deck to Repository (R2R) Cruise doi:10.7284/904028 (TN272) and 10.7284/904324 (SKQ20142S) and the Marine Geoscience Data System (http://www.marine-geo.org/index.php).

Acknowledgments
We thank the captains and crews on R/V Thomas G. Thompson (TN272) and R/V Sikuliaq (SKQ20142S) as well as all the Sentry AUV engineers onboard and on-shore for making the deepwater, long-range marathon dives over the two expeditions possible. We also thank leading Co-Pis, Professor Adrienne Oakley and Dr Daniel Lizarralde, and all the participants whose watchstanding made these two cruises successful. We thank JGR Associate Editor Isabelle Manighetti, two anonymous reviewers, and JGR Associate Editor Mark Dekkers for their constructive comments that improved the clarity of the manuscript. This study is funded by National Science Foundation grants OCE-1029965 (Tominaga, Tivey, and Lizarralde) and OCE-1233000 (Tominaga and Tivey) and OCE-1029573 (Sager).

References

Abrams, L. J., Larson, R. L., Shipley, T. H., & Lancelot, Y. (1992). *The seismic stratigraphy and sedimentary history of the East Mariana and Pigafetta Basins of the western Pacific*. In R. L. Larson, Y. Lancelot, A. Fisher, & E. L. Winterer (Eds.), Proceedings of the Ocean Drilling Program, Scientific Results (129, pp. 551–561). College Station, TX: Ocean Drilling Program.

Baksi, A. K., & Hoffman, K. A. (2000). On the age and morphology of the Reunion Event. *Geophysical Research Letters*, *27*, 2997–3000.

Barrett, D. L., & Keen, C. E. (1976). Mesozoic magnetic lineations, the magnetic quiet zone, and sea floor spreading in the northwest Atlantic. *Journal of Geophysical Research*, *81*, 4875–4884.

Bartolini, A., & Larson, R. L., (2001). Pacific microplate and the Pangea supercontinent in the Early to Middle Jurassic: *Geology*, *29*, 735–738.

Biggin, A. J., Piispa, E., Pesonen, L., Holme, R., Paterson, G., Veikkolainen, T., & Tauxe, L. (2015). Paleomagnetic field intensity variations suggest mesoproterozoic inner-core nucleation. *Nature*, *526*(7572), 245–248.

Biggin, A. J., & Thomas, D. N. (2003). Analysis of long-term variations in the geomagnetic poloidal field intensity and evaluation of their relationship with global geodynamics. *Geophysical Journal International*, *152*, 392–415.

Biggin, A. J., van Hinsbergen, D. J. J., Langereis, C. G., Straathof, G. B., & Deenen, M. H. L. (2008). Geomagnetic secular variation in the Cretaceous normal superchron and in the Jurassic. *Physics of the Earth and Planetary Interiors*, *169*, 3–19.

Bono, R. K., Tarduno, J. A., Nimmo, F., & Cottrell, R. D. (2019). Young inner core inferred from Ediacaran ultra-low geomagnetic field intensity. *Nature Geoscience*, *12*, 143–147.

Boschman, L. M., & van Hinsbergen, D. J. J. (2016). On the enigmatic birth of the Pacific Plate within the Panthalassa Ocean. *Science Advances*, *2*, e1600022.

Bowers, N. E., Cande, S. C., Gee, J. S., Hildebrand, A., & Parker, R. L. (2001). Fluctuations of the paleomagnetic field during Chron C5 as recorded in near-bottom marine magnetic anomaly data. *Journal of Geophysical Research*, *106*, 26379–26396.

Bowles, J., Tauxe, L., Gee, J., McMillan, D., & Cande, S. (2003). Source of tiny wiggles in Chron C5: A comparison of sedimentary relative intensity and marine magnetic anomalies. *Geochemistry, Geophysics, Geosystems*, *4*(6), 1049. https://doi.org/10.1029/2002GC000489

Buffett, B. A. (2000). Earth's core and the geodynamo. *Science*, *288*, 2007–2012.
Cande, S. C., & Kent, D. V. (1992). A new geomagnetic polarity time scale for the Late Cretaceous and Cenozoic. *Journal of Geophysical Research*, *97*, 13917–13951.
Cande, S. C., & Kent, D. V. (1992). Ultrahigh resolution marine magnetic anomaly profiles: A record of continuous paleointensity variations? *Journal of Geophysical Research*, *97*, 15075–15083.
Cande, S. C., & Kent, D. V. (1995). Revised calibration of the geomagnetic polarity timescale for the late Cretaceous and Cenozoic. *Journal of Geophysical Research*, *100*, 6093–6095.
Cande, S. C., Larson, R. L., & LaBrecque, J. L. (1978). Magnetic lineations in the Pacific Jurassic Quiet Zone. *Earth and Planetary Science Letters*, *41*, 434–440.
Channell, J. E. T., Erba, E., Nakanishi, M., & Tamaki, K. (1995). *Late Jurassic–Early Cretaceous time scales and oceanic magnetic anomaly block models*. In W. A. Berggren, D. V. Kent, M.-P. Aubry, & J. Hardenbol (Eds.), Geochronology, time scales and global stratigraphic correlation (54, pp. 51–63), Spec. Pub. Tulsa, OK: SEPM (Society for Sedimentary Geology).
Channell, J. E. T., Labs, J., & Raymo, M. E. (2003). The Réunion Subchronozone at ODP Site 981 (Feni Drift, North Atlantic). *Earth and Planetary Science Letters*, https://doi.org/10.1016/S0012-821X(03)00435-7.
Channell, J. E. T., Singer, B. S., & Jicha, B. R. (2020). Timing of Quaternary geomagnetic reversals and excursions in volcanic and sedimentary archives. *Quaternary Science Reviews*, *228*, https://doi.org/10.1016/j.quascirev.2019.106114.
Clouard, V., & Bonneville, A. (2004). *Ages of seamounts, islands and plateaus on the Pacific plate*. In G. R. Foulger, J. H. Natland, D. C. Presnall, & D. L. Anderson (Eds.), Plates, plumes and paradigms (388, pp. 71–90), Special Paper. Boulder, CO: Geological Society of America.
Coe, R. S., & Glatzmaier, G. A. (2006). Symmetry and stability of the geomagnetic field. *Geophysical Research Letters*, *33*, L21311. https://doi.org/10.1029/2006GL027903
Coe, R. S., Hongre, L., & Glatzmaier, G. (2000). An examination of simulated geomagnetic polarity reversals. *Proceedings of the Royal Society of London*, *358*(1768), 1141–1170.
Coffin, M. F., Lawver, L. A., Gahagan, L. M., & Campbell, D. A. (2000). The Plates Project 2000 atlas of plate reconstructions (750 Ma to present day) (Plates Project Progress Report, 250, 89 pp.). Austin, TX: University of Texas.
Constable, C. (2003). Geomagnetic reversals: Rates, timescales, preferred paths, statistical models and simulations. In C. A. Jones, A. M. Soward, & K. Zhang (Eds.), The fluid mechanics of astrophysics and geophysics, Earth's core and lower mantle (Vol. 11, pp. 96–122). London and New York: Taylor & Francis.
Cooper, A. K., Marlow, M. S., & Scholl, D. W. (1976). Mesozoic magnetic lineations in the Bering Sea marginal basin. *Journal of Geophysical Research*, *81*, 1916–1934.
Courtillot, V., & Besse, J. (1987). Magnetic field reversals, polar wander, and core–mantle coupling. *Science*, *237*, 1140–1147.
Cox, A. (1969). Geomagnetic Reversals. *Science*, *163*(3864), 237–245.
Cronin, M., Tauxe, L., Constable, C., Selkin, P., & Pick, T. (2001). Noise in the quiet zone. *Earth and Planetary Science Letters*, *190*, 13–30.
Deenen, M. H. L., Krijgsman, W., & Ruhl, M. (2011). The quest for Chron E23r at Partridge Island, Bay of Fundy, Canada: CAMP emplacement postdates the end-Triassic extinction event at the North American craton. *Canadian Journal of Earth Sciences*, *48*, 1282–1291.
Dormy, E., Valet, J.-P., & Courtillot, V. (2000). Numerical models of the geodynamo and observational constraints. *Geochemistry, Geophysics, Geosystems*, *1*, 2000GC000062.
Erba, E., Duncan, R. A., Bottini, C., Tiraboschi, D., Weissert, H., Jenkyns, H. C., & Malinverno, A. (2015). Environmental consequences of Ontong Java Plateau and Kerguelen Plateau volcanism. In *Geological Society of America Special Paper 511* (pp. 271–303). Boulder, CO: Geological Society of America. https://doi.org/10.1130/2015.2511(15)
Feng, H. S. (2016). *Seismic constraints on the processes and consequences of secondary igneous evolution of Pacific Oceanic Lithosphere*, Cambridge, Massachusetts: (PhD dissertation). Massachusetts Institute of Technology.
Feng, H. S., Lizarralde, D., Hart, L. A., Tominaga, M., Tivey, M. A., & Swift, S. A. (2015). Extent and impact of Cretaceous magmatism on the formation and evolution of Jurassic oceanic crust in the western Pacific. In *Abstract (V21A-3016) presented at 2015 Fall Meeting, AGU* (Abstract GP23B-1310). San Francisco.
Gee, J. S., & Kent, D. V. (2007). Source of oceanic magnetic anomalies and the geomagnetic polarity time scale. *Treatise on Geophysics*, *5*, 455–507.
Gipe, R. A. (2013). *Callovian (upper Middle Jurassic) magnetostratigraphy: A composite polarity pattern from France, Britain and Germany, and its correlation to the Pacific marine magnetic anomaly model*, West Lafayette, Indiana: (open access theses, Paper 36). Purdue University.
Glatzmaier, G. A. (2002). Geodynamo simulations—How realistic are they? *Annual Review of Earth and Planetary Sciences*, *30*(1), 237–257.
Glatzmaier, G. A., & Roberts, P. H. (1995). A three-dimensional self-consistent computer simulation of a geomagnetic field reversal. *Nature*, *377*, 203–209.
Gradstein, F. M., Ogg, J. G., Schmitz, M., & Ogg, G. (2012). *The Geological Time Scale 2012* (pp. 1176). Oxford, UK: Elsevier.
Granot, R., Dyment, J., & Gallet, Y. (2012). Geomagnetic field variability during the Cretaceous normal superchron. *Nature Geoscience*, *5*(3), 220–223.
Granot, R., Tauxe, L., Gee, J. S., & Ron, H. (2007). A view into the Cretaceous geomagnetic field from analysis of gabbros and submarine glasses. *Earth and Planetary Science Letters*, *256*, 1–11.
Gurevich, N. I., Merkur'ev, S. A., & Sbel'skaya, A. A. (2006). Evolution of the southern part of the Canada Basin (Arctic Ocean) based on magnetometric data. *Doklady Earth Sciences*, *407*, 308–311.
Guspi, F. (1987). Frequency-Domain reduction of potential field measurements to a horizontal plane. *Geoexploration*, *24*, 87–89.
Hamilton, E. L. (1956). Sunken Islands of the Mid-Pacific Mountains. *Geological Society of America Bulletin Memoir*, *64*, 1–92.
Handschumacher, D. W., Sager, W. W., Hilde, T. W. C., & Bracey, D. R. (1988). Pre-Cretaceous tectonic evolution of the Pacific plate and extension of the geomagnetic polarity reversal timescale with implications for the origin of the Jurassic "Quiet Zone". *Tectonophysics*, *155*, 365–380.
Hayes, D. E., & Rabinowitz, P. D. (1975). Mesozoic magnetic lineations and the magnetic quiet zone off Northwest Africa. *Earth and Planetary Science Letters*, *28*, 105–115.
He, H., Pan, Y. X., Tauxe, L., Qin, H. F., & Zhu, R. X. (2008). Toward age determination of the M0r (Barremian–Aptian boundary) of the Early Cretaceous. *Physics of the Earth and Planetary Interiors*, *169*, 41–48.
Heirtzler, J. R., & Hayes, D. E. (1967). Magnetic boundaries in the North Atlantic Ocean. *Science*, *157*(3785), 185–187.
Hilde, T. W. C., Uyeda, S., & Kroenke, L. (1976). Tectonic history of the Western Pacific. In C. L. Drake (Ed.), *Geodynamics: Progress and prospects*. Washington, DC: American Geophysical Union. https://doi.org/10.1029/SP005p0001

Hounslow, M. W., Domeier, M., & Biggin, A. J. (2018). Subduction flux modulates the geomagnetic polarity reversal rate. *Tectonophysics*, *742–743*, 34–49.

Ingham, E., Heslop, D., Roberts, A. P., Hawkins, R., & Sambridge, M. (2014). Is there a link between geomagnetic reversal frequency and paleointensity? A Bayesian approach. *Journal of Geophysical Research: Solid Earth*, *119*, 5290–5304. https://doi.org/10.1002/2014JB010947

Kaneda, K., Kodaira, S., Nishizawa, A., Morishita, T., & Takahashi, N. (2010). Structural evolution of preexisting oceanic crust through intraplate igneous activities in the Marcus-Wake seamount chain. *Geochemistry, Geophysics, Geosystems*, *11*, Q10014. https://doi.org/10.1029/2010GC003231

Kent, D. V., & Gradstein, F. M. (1985). A Cretaceous and Jurassic geochronology. *The Geological Society of America Bulletin*, *96*(11), 1419–1427.

Kent, D. V., & Olsen, P. E. (1999). Astronomically tuned geomagnetic polarity timescale for the Late Triassic. *Journal of Geophysical Research*, *104*, 12831–12841.

Kent, D. V., & Olsen, P. E. (2008). Early Jurassic magnetostratigraphy and paleolatitudes from the Hartford continental rift basin (eastern North America): Testing for polarity bias and abrupt polar wander in association with the central Atlantic magmatic province. *Journal of Geophysical Research*, *113*, B06105. https://doi.org/10.1029/2007JB005407

Kent, D. V., Olsen, P. E. ., & Muttoni, G. (2017). Astrochronostratigraphic polarity time scale (APTS) for the Late Triassic and Early Jurassic from continental sediments and correlation with standard Marine Stages. *Earth-Science Reviews*, *166*, 153–180.

Klitgord, K. D., & Schouten, H. (1986). Plate kinematics of the central Atlantic. In P. R. Vogt & B. E. Tucholke (Eds.), *The geology of North America, Volume M. The Western North Atlantic region* (pp. 351–378). Boulder, CO: Geological Society of America.

Knudsen, M. F., Holm, P. M., & Abrahamsen, N. (2009). Paleomagnetic results from a reconnaissance study of Santiago (cape Verde Islands): Identification of cryptochron C2r.2r-1. *Physics of the Earth and Planetary Interiors*, *173*, 279–289.

Koppers, A., Staudigel, H., & Duncan, R. A. (2003). High resolution $^{40}Ar/^{39}Ar$ dating of the oldest oceanic basement basalts in the western Pacific basin. *Geochemistry, Geophysics, Geosystems*, *4*(11), 8914. https://doi.org/10.1029/2003GC000574

Koppers, A., Staudigel, H., Pringle, M. S., & Wijbrans, J. R. (2003). Short-lived and discontinuous intraplate volcanism in the South Pacific: Hot spots or extensional volcanism? *Geochemistry, Geophysics, Geosystems*, *4*(10), 1089. https://doi.org/10.1029/2003GC000533

Korenaga, J. (1995). Comprehensive analysis of marine magnetic vector anomalies. *Journal of Geophysical Research*, *100*, 365–378. https://doi.org/10.1029/94JB02596

Kulakov, E. V., Sprain, C. J., Doubrovine, P. V., Smirnov, A. V., Paterson, G. A., Hawkins, L. L., et al. (2019). Analysis of an updated paleointensity database (QPI-PINT) for 65–200 Ma: Implications for the long-term history of dipole moment through the Mesozoic, *Journal of Geophysical Research: Solid Earth*, *124*, 9999–10022. https://doi.org/10.1019/2018JB017287

Lancelot, Y., Larson, R. L., & Fisher, A. (1990). Ocean Drilling Program Leg 129 preliminary report: Old Pacific Crust. *Proceedings of Ocean Drilling Program, Scientific Results*, *129*, 1–28.

Lancelot, Y., Larson, R. L., & Shipboard Scientific Party. (1990). Proceedings of Ocean Drilling Program, Scientific Results (129). College Station, TX: Ocean Drill. Program.

Lanci, L., & Lowrie, W. (1997). Magnetostratigraphic evidence that 'tiny wiggles' in the oceanic magnetic anomaly record represent geomagnetic paleointensity variations. *Earth and Planetary Science Letters*, *148*, 581–592.

Larson, R. L. (1991). Latest pulse of Earth: Evidence for a mid-Cretaceous superplume. *Geology*, *19*, 547–550. https://doi.org/10.1130/0091-7613(1991)019<0547:LPOEEF>2.3.CO;2

Larson, R. L., & Chase, C. G. (1972). Late Mesozoic evolution of the western Pacific Ocean. *The Geological Society of America Bulletin*, *83*, 3627–3644.

Larson, R. L., & Hilde, T. W. C. (1975). A revised timescale of magnetic reversals for the Early Cretaceous and Late Jurassic. *Journal of Geophysical Research*, *80*, 2586–2594.

Larson, R. L., & Olson, P. (1991). Mantle plumes control magnetic reversal frequency. *Earth and Planetary Science Letters*, *107*, 437–447. https://doi.org/10.1016/j.epsl.2011.09.015

Larson, R. L., & Pitman, W. C. (1972). World-wide correlation of Mesozoic magnetic anomalies, and its implications. *The Geological Society of America Bulletin*, *83*(12), 3645–3662. https://doi.org/10.1130/0016-7606

Larson, R. L., & Sager, W. W. (1992). Skewness of magnetic anomalies M0 to M29 in the northwestern Pacific. *Proceedings of Ocean Drilling Program, Scientific Results*, *129*, 471–481.

Leinweber, V. T., & Jokat, W. (2012). The Jurassic history of the Africa–Antarctica corridor—New constraints from magnetic data on the conjugate continental margins. *Tectonophysics*, *530–531*, 87–101.

Llanos, M. P. I., Kietzmann, D. A., Martínez, M. K., & Minisini, D. (2019). Magnetostratigraphy of a Middle Jurassic delta system (Lajas Formation), Portada Covunco section, southern Neuquén Basin, Argentina. *Journal of South American Earth Sciences*, *94*(2019), 102235.

Lowrie, W., & Channell, J. E. T. (1984). Magnetostratigraphy of the Jurassic–Cretaceous boundary in the maiolica limestone (Umbria, Italy). *Geology*, *12*, 44–47.

Lowrie, W., & Kent, D. V. (2004). Timescales of the Paleomagnetic field. In *AGU Geophysical Monograph* (Vol. 145). Washington D.C.: AGU. https://doi.org/10.1029/145GM09

Ludden, J. (1992). Radiometric age determinations for basement from Site 765 and 766, Argo abyssal plain and north western Australia. *Proceedings of Ocean Drilling Program, Scientific Results*, *123*, 557–559.

Madrigal, P., Gazel, E., Flores, K. E., Bizimis, M., & Jicha, B. (2016). Record of massive upwellings from the Pacific large low shear velocity province. *Nature Communications*, *7*, 13309.

Malinverno, A., Hildebrandt, J., Tominaga, M., & Channell, J. E. T. (2012). M-sequence geomagnetic polarity time scale (MHTC12) that steadies global spreading rates and incorporates astrochronology constraints. *Journal of Geophysical Research: Solid Earth*, *117*, B06104. https://doi.org/10.1029/2012JB009260

McElhinny, M., & Larson, R. L. (2003). Jurassic dipole low defined from land and sea data. *Eos, Transactions, American Geophysical Union*, *84*, 362–366.

McFadden, P. L., & Merrill, R. T. (1993). Inhibition and geomagnetic field reversals. *Journal of Geophysical Research*, *98*, 6189–6199. https://doi.org/10.1029/92JB02574

McFadden, P. L., Merrill, R. T., McElhinny, M. W., & Lee, S. H. (1991). Reversals of the Earth's magnetic-field and temporal variations of the dynamo families. *Journal of Geophysical Research*, *96*, 3923–3933.

Meyer, B., Saltus, R., & Chulliat, A. (2017). EMAG2: Earth Magnetic Anomaly Grid (2-arc-minute resolution) version 3. *NOAA National Centers for Environmental Information. https://doi.org/10.7289/V5H70CVX. Accessed [2021].* https://doi.org/10.7289/V5H70CVX

Mochizuki, K., Coffin, M. F., Eldholm, O., & Taira, A. (2005). Massive Early Cretaceous volcanic activity in the Nauru Basin related to emplacement of the Ontong Java Plateau. *Geochemistry, Geophysics, Geosystems*, *6*, Q10003. https://doi.org/10.1029/2004GC000867

Morgan, W. J. (1972). Deep mantle convection plumes and plate motions. *American Association of Petroleum Geologists*, *56*(2), 203–213.
Müller, R. D., Seton, M., Zahirovic, S., Williams, S. E., Matthews, K. J., Wright, N. M., et al. (2016). Ocean basin evolution and global-scale plate reorganization events since Pangea breakup. *Annual Review of Earth and Planetary Sciences*, *44*, 107–138.
Nakanishi, M., Tamaki, K., & Kobayashi, K. (1989). Mesozoic magnetic anomaly lineations and seafloor spreading history of the northwestern Pacific. *Journal of Geophysical Research*, *94*, 15437–15462.
Nakanishi, M., Tamaki, K., & Kobayashi, K. (1992). Magnetic anomaly lineations from late Jurassic to Early Cretaceous in the west central Pacific Ocean. *Geophysical Journal International*, *109*, 701–719.
Nakanishi, M., & Winterer, E. L. (1998). Tectonic history of the Pacific–Farallon–Phoenix triple junction from Late Jurassic to Early Cretaceous: An abandoned Mesozoic spreading system in the Central Pacific Ocean. *Journal of Geophysical Research*, *103*, 12453–12468.
Ogg, J. G., Chunju, H., Hinnov, L. A., & Gradstein, F. M. (2018). *Age model for Late Jurassic through Early Cretaceous used in the geologic timescale 2012/2016 reference scales*. Paper presented at GSA Ann. Meeting, USA 2018, Paper No. 241-1.
Ogg, J. G., Coe, A. L., Przybylski, P. A., & Wright, J. K. (2010). Oxfordian magnetostratigraphy of Britain and its correlation to Tethyan regions and Pacific marine magnetic anomalies. *Earth and Planetary Science Letters*, *289*, 433–338.
Ogg, J. G., & Gutowski, J. (1995). Oxfordian magnetic polarity time scale. In A. C. Riccardi (Ed.), *Proceedings of the 4th International Congress on Jurassic Stratigraphy and Geology, Geo. Res. Forum v. 1–2* (pp. 406–414). Zurich, Switzerland: Trans-Tec Publications Ltd.
Ogg, J. G., Karl, S. M., & Behl, R. J. (1992). Jurassic through Early Cretaceous sedimentation history of the central equatorial Pacific and of Sites 800 and 801. *Proceedings of the Ocean Drilling Program, Scientific Results*, *129*, 571–613.
Ogg, J. G., Ogg, G. M., & Gradstein, F. M. (2016). *A concise geologic time scale: 2016* (pp. 240). Amsterdam, Netherland: Elsevier.
Ohira, A., Kodaira, S., Nakamura, Y., Fujie, G., Arai, R., & Miura, S. (2017). Structural variation of the oceanic Moho in the Pacific plate revealed by active-source seismic data. *Earth and Planetary Science Letters*, *476*, 111–121.
Olierook, H. K. H., Jourdan, F., & Merle, R. E. (2019). Age of the Barremian–Aptian boundary and onset of the Cretaceous Normal Superchron. *Earth-Science Reviews*, *197*, 102906.
Olson, P., & Amit, H. (2015). Mantle superplumes induce geomagnetic superchrons. *Frontiers of Earth Science*, *3*(38). https://doi.org/10.3389/feart.2015.00038
Olson, P., Christensen, U., & Glatzmaier, G. A. (1999). Numerical modeling of the geodynamo mechanisms of field generation and equilibration. *Journal of Geophysical Research*, *104*, 10383–10404.
Olson, P., Deguen, R., Hinnov, L. A., & Zhong, S. (2013). Controls on geomagnetic reversals and core evolution by mantle convection in the Phanerozoic. *Physics of the Earth and Planetary Interiors*, *214*, 87–103.
Otofuji, Y., Zaman, H., Shimoda, M., Aihara, K., Kani, M., Yokoyama, M., et al. (2013). Recognition of 'cryptochron' in the polarity subchron C3Ar: Paleomagnetic results of the late Miocene lava sequence from Noma Peninsula (Kyushu island), Japan. *Geophysical Journal International*, *193*, 122–135.
Parker, R. L. (1972). The rapid calculation of potential field anomalies. *Geophysical Journal of the Royal Astronomical Society*, *31*, 447–455.
Parker, R. L., & Huestis, S. P. (1974). The inversion of magnetic anomalies in the presence of topography. *Journal of Geophysical Research*, *79*, 1587–1593.
Petronotis, K. E., & Gordon, R. G. (1989). Age dependence of skewness of magnetic anomalies above seafloor formed at the Pacific-Kula spreading center. *Geophysical Research Letters*, *16*(4), 315–318.
Plank, T., Ludden, J. N., Escutia, C., & Shipboard Scientific Party. (2000). *Site 801, Proceedings of Ocean Drilling Program, Initial Reports* (185 [CD-ROM]). College Station, TX: Ocean Drilling Program, Texas A&M University.
Pockalny, R. A., & Larson, R. L. (2003). Implications for crustal accretion at fast spreading ridges from observations in Jurassic oceanic crust in the western Pacific. *Geochemistry, Geophysics, Geosystems*, *4*(1), 8903. https://doi.org/10.1029/2001GC000274
Prévot, M., Derder, M. E. M., McWilliams, & Thompson, J. (1990). Intensity of the Earth's magnetic field: Evidence for a Mesozoic Dipole Low. *Earth and Planetary Science Letters*, *97*, 129–139.
Przybylski, P. A., Ogg, J. G., Wilerzbowski, A., Cole, A. L., Hounslow, M. W., Wright, J. K., et al. (2010a). Magnetostratigraphic correlation of the Oxfordian-Kimmeridgian1021 boundary. *Earth and Planetary Science Letters. 239*, 256–272.
Przybylski, P. A., Głowniak, E., Ogg, J.G., Ziółkowski, P., Sidorczuk, M., Gutowski, J., & Lewandowski, M., (2010b). Oxfordian magnetostratigraphy of Poland and its correlation to Sub-Mediterranean ammonite zones and marine magnetic anomalies. *Earth and Planetary Science Letters*, *289*, 417–432.
Ramana, M. V., Nair, R. R., Sarma, K. V. L. N. S., Ramprasad, T., Krishna, K. S., Subrahmanyam, V., et al. (1994). Mesozoic anomalies in the Bay of Bengal. *Earth and Planetary Science Letters*, *121*, 469–475.
Ramana, M. V., Ramprasad, T., & Desa, M. (2001). Seafloor spreading magnetic anomalies in the Enderby Basin, East Antarctica. *Earth and Planetary Science Letters*, *191*, 241–255.
Roberts, A. P., & Lewin-Harris, J. C. (2000). Marine magnetic anomalies: Evidence that 'tiny wiggles' represent short-period geomagnetic polarity intervals. *Earth and Planetary Science Letters*, *183*, 375–388.
Roeser, H. A., Steiner, C., Schreckenberger, B., & Block, M. (2002). Structural development of the Jurassic Magnetic Quiet Zone off Morocco and identification of Middle Jurassic magnetic lineations. *Journal of Geophysical Research*, *107*(B10), 2207. https://doi.org/10.1029/2000JB000094
Roest, W. R., Danobeitia, J. J., Verhoef, J., & Collette, B. J. (1992). Magnetic anomalies in the Canary basin and the Mesozoic evolution of the central north Atlantic. *Marine Geophysical Researches*, *14*, 1–24.
Ryan, W. B. F., Carbotte, S. M., Coplan, J. O., O'Hara, S., Melkonian, A., Arko, R., et al. (2009). Global multi-resolution topography synthesis. *Geochemistry, Geophysics, Geosystems*, *10*, Q03014. https://doi.org/10.1029/2008GC002332
Rybakov, M., Goldshmidt, V., Fleischer, L., & Ben-Gai, Y. (2000). 3-D gravity and magnetic interpretation for the Haifa Bay area (Israel). *Journal of Applied Geophysics*, *44*, 353–367.
Sager, W. W., Fullerton, L. G., Buffler, R. T., & Handschumacher, D. W. (1992). Argo Abyssal Plain magnetic lineations revisited: Implications for the onset of seafloor spreading and tectonic evolution of the eastern Indian ocean. *Proceedings of Ocean Drilling Program, Scientific Results*, *123*, 659–669.
Sager, W. W., Weiss, C. J., Tivey, M. A., & Johnson, H. P. (1998). Geomagnetic polarity reversal model of deep-tow profiles from the Pacific Jurassic Quiet Zone. *Journal of Geophysical Research*, *103*, 5269–5286.
Saito, K., & Ozima, M. (1977). ^{40}Ar–^{39}Ar geochronological studies on submarine rocks from the western Pacific area. *Earth and Planetary Science Letters*, *33*, 353–369.
Schlanger, S., & Moberly, R. (1986). Sedimentary and volcanic history: East Mariana and Nauru Basin. *Initial Reports of the Deep Sea Drilling Project*, *586*, 653–678.
Schouten, H., & McCamy, K. (1972). Filtering marine magnetic anomalies. *Journal of Geophysical Research*, *77*(35), 7089–7099.

Seton, M., Müller, R. D., Zahirovic, S., Gaina, C., Torsvik, T., Shephard, G., et al. (2012). Global continental and ocean basin reconstructions since 200 Ma. *Earth-Science Reviews*, *113*, 212–270.

Singer, B. S., Jicha, B. R., Condon, D. J., Macho, A. S., Hoffman, K. A., Dierkhising, J., et al. (2014). Precise ages of the Réunion event and Huckleberry Ridge excursion: Episodic clustering of geomagnetic instabilities and the dynamics of flow within the outer core. *Earth and Planetary Science Letters*, *405*, 25–38.

Smirnov, A. V., Kulakov, E. V., Foucher, M. S., & Bristol, K. E. (2017). Intrinsic paleointensity bias and the long-term history of the geodynamo. *Science Advances*, *3*, e1602306.

Smith, D. K., & Jordan, T. H. (1987). The size distribution of Pacific seamounts. *Geophysical Research Letters*, *14*, 1119–1122.

Smith, D. K., & Jordan, T. H. (1988). Seamount statistics in the Pacific Ocean. *Journal of Geophysical Research*, *93*, 2899–2918.

Smith, W. H. F., & Sandwell, D. T. (1997). Global seafloor topography from satellite altimetry and ship depth soundings. *Science*, *277*, 1957–1962.

Stadler, T. J., & Tominaga, M. (2015). Intraplate volcanism of the western Pacific: New insights from geological and geophysical observations in the Pigafetta Basin. *Geochemistry, Geophysics, Geosystems*, *16*, 3015–3033. https://doi.org/10.1002/2015GC005873

Steiner, M. B. (2001). Tango in the Mid-Jurassic: 10,000-yr geomagnetic field reversals. *Eos, Transactions, American Geophysical Union*, *82*(47), Fall Meet. Suppl., Abstract GP12A-0205.

Steiner, M. B., Ogg, J. G., Melendez, G., & Sequeiros, L. (1985). Jurassic magnetostratigraphy, 2. Middle-Late Oxfordian of Aguilon, Iberian Cordillera, northern Spain. *Earth and Planetary Science Letters*, *76*, 151–166.

Steiner, M. B., Ogg, J., & Sandoval, J. (1987). Jurassic magnetostratigraphy, 3. Bathonian-Bajocian of Carcabuey, Sierra Harana and Campillo de Arenas (Subbetic Cordillera, Southern Spain). *Earth and Planetary Science Letters*, *82*, 357–372.

Takahashi, F., Matsushima, M., & Honkura, Y. (2005). Simulations of a quasi-Taylor state geomagnetic field including polarity reversals on the Earth simulator. *Science*, *309*, 459–461.

Talwani, M., & Heirtzler, J. R. (1964). Computation of magnetic anomalies caused by two-dimensional structures of arbitrary shape. In G. A. Parks (Ed.), *Computers in the mineral industries* (pp. 464–480). Stanford, CA: Stanford University Press.

Tarduno, J. A., & Cottrell, R. D. (2005). Dipole strength and variation of the time-averaged reversing and nonreversing geodynamo based on Thellier analyses of single plagioclase crystals. *Journal of Geophysical Research*, *110*, B11101. https://doi.org/10.1029/2005JB003970

Tarduno, J. A., Cottrell, R. D., & Smirnov, A. V. (2001). High geomagnetic intensity during the Mid-Cretaceous from Thellier analyses of single plagioclase crystals. *Science*, *291*, 1779–1783.

Tarduno, J. A., Cottrell, R. D., & Smirnov, A. V. (2006). The paleomagnetism of single silicate crystals: Recording geomagnetic field strength during mixed polarity intervals, superchrons, and inner core growth. *Reviews of Geophysics*, *41*, RG1002. https://doi.org/10.1029/2005RG000189

Tauxe, L. (2006). Long-term trends in paleointensity: The contribution of DSDP/ODP submarine basaltic glass collections. *Physics of the Earth and Planetary Interiors*, *156*, 223–241.

Tauxe, L., Gee, J. S., Steiner, M. B., & Staudigel, H. (2013). Paleointensity results from the Jurassic: New constraints from submarine basaltic glasses of ODP Site 801C. *Geochemistry, Geophysics, Geosystems*https://doi.org/10.1002/ggge.20282

Thebault, E., Finlay, C., Beggan, C., Alken, P., Aubert, J., Barrois, O., et al. (2015). International Geomagnetic Reference Field: The 12th generation. *Earth Planets and Space*, *67*, 79. https://doi.org/10.1186/s40623-015-0228-9

Thomas, D. N., & Biggin, A. J. (2003). Does the Mesozoic dipole low really exist? *Eos, Transactions, American Geophysical Union*, *84*(97), 103–104.

Tivey, M. A., Larson, R. L., Pockalny, R., & Schouten, H. (2005). Downhole magnetic measurements of ODP Hole 801C: Implications for Pacific oceanic crust and magnetic field behavior in the Middle Jurassic. *Geochemistry, Geophysics, Geosystems*, *6*, Q04008. https://doi.org/10.1029/2004GC000754

Tivey, M. A., Sager, W. W., Lee, S., & Tominaga, M. (2006). Rapid magnetic field reversal and low amplitude as a cause of the Pacific Jurassic Quiet Zone. *Geology*, *34*(9), 789–792. https://doi.org/10.1130/G22849

Tominaga, M., & Sager, W. W. (2010). Revised Pacific M-anomaly geomagnetic polarity time scale, *Geophysical Journal International*, *182*, 203–232.

Tominaga, M., Sager, W. W., Tivey, M. A., & Lee, S. M. (2008). Deep-tow magnetic anomaly study of the Pacific Jurassic Quiet Zone and implications for the geomagnetic polarity reversal timescale and geomagnetic field behavior. *Journal of Geophysical Research*, *113*, B07110. https://doi.org/10.1029/2007JB005527

Tominaga, M., Tivey, M. A., & Sager, W. W. (2015). Nature of the Jurassic magnetic Quiet Zone. *Geophysical Research Letters*, *42*, 8367–8372. https://doi.org/10.1002/2015GL065394

Valet, J.-P., & Fournier, A. (2016). Deciphering records of geomagnetic reversals. *Reviews of Geophysics*, *54*, 410–446. https://doi.org/10.1002/2015RG00050

Van Avendonk, H., Davis, J., Harding, J., & Lawver, L. (2017). Decrease in oceanic crustal thickness since the breakup of Pangaea. *Nature Geoscience*, *10*, 58–61.

Verhoef, J., & Scholten, R. D. (1983). Cross-over analysis of marine magnetic anomalies. *Marine Geophysical Researches*, *5*, 421–435.

Vogt, P. R., Anderson, C. N., & Bracey, D. R. (1971). Mesozoic magnetic anomalies, sea-floor spreading, and geomagnetic reversals in the southwestern North Atlantic. *Journal of Geophysical Research*, *76*, 4796–4823. https://doi.org/10.1029/JB076i020p04796

Vogt, P. R., & Einwich, A. M. (1979). Magnetic anomalies and sea-floor spreading in the western north Atlantic, and a revised calibration of the Keathley (*M*) geomagnetic reversal chronology. *Initial Reports of the Deep Sea Drilling Project*, *43*, 857–876.

Walker, J. D., Geissman, J. W., Bowring, S. A., & Babcock, L. E. (2013). The Geological Society of America geologic time scale. *GSA Bulletin*, *125*, 259–272.

Woods, M. T., & Davies, G. F. (1982). Late Cretaceous genesis of the Kula plate. *Earth and Planetary Science Letters*, *58*(2), 161–166. https://doi.org/10.1016/0012-821X(82)90191-1

Zelt, C. A., & Smith, R. B. (1992). Seismic traveltime inversion for 2-D crustal velocity structure. *Geophysical Journal International*,*108*, 16–34.

Zhang, N., & Zhong, S. J. (2011). Heat fluxes at the Earth's surface and core–mantle boundary since Pangea formation and their implications for the geomagnetic superchrons. *Earth and Planetary Science Letters*, *306*, 205–216.

Zhang, Y., Ogg, J. G., Minguez, D. A., Hounslow, M., Olaussen, S., Gradstein, F., & Esmeray-Senlet, S. (2019). Magnetostratigraphy of U/Pb-dated boreholes in Svalbard, Norway, implies that the Barremian–Aptian boundary (beginning of Chron M0r) is 121.2±0.4 Ma. In *AGU Fall Meeting*, Abstracts (Vol. 2019, pp. GP44A-06). San Francisco.